https://doi.org/10.5194/essd-2022-211
Preprint. Discussion started: 4 July 2022

High-resolution physicochemical dataset of atmospheric aerosols over the Tibetan Plateau and its surroundings

Xinghua Zhang[1,⋆], Wenhui Zhao[1,2,⋆], Lixiang Zhai[1,2], Miao Zhong[1,2], Jinsen Shi[3], Junying Sun[4], Yanmei Liu[1,a], Conghui Xie[1,b], Yulong Tan[1,2], Kemei Li[1,2], Xinlei Ge[5], Qi Zhang[6], Shichang Kang[1,2,7], Jianzhong Xu[1,*]

[1]State Key Laboratory of Cryospheric Sciences, Northwest Institute of Eco-Environment and Resources, Chinese Academy of Sciences, Lanzhou 730000, China

[2]University of Chinese Academy of Sciences, Beijing 100049, China

[3]Key Laboratory for Semi-Arid Climate Change of the Ministry of Education, College of Atmospheric Sciences, Lanzhou University, Lanzhou 730000, China

[4]Key Laboratory of Atmospheric Chemistry of CMA, Chinese Academy of Meteorological Sciences, Beijing 100081, China

[5]Jiangsu Key Laboratory of Atmospheric Environment Monitoring and Pollution Control, Collaborative Innovation Center of Atmospheric Environment and Equipment Technology, School of Environmental Science and Engineering, Nanjing University of Information Science and Technology, Nanjing 210044, China

[6]Department of Environmental Toxicology, University of California, Davis, CA 95616, USA

[7]CAS Center for Excellence in Tibetan Plateau Earth Sciences, Beijing 100085, China

[a]now at: Department of Environmental Science and Engineering, Sichuan University, Chengdu 610065, China

[b]now at: State Key Joint Laboratory of Environmental Simulation and Pollution Control, College of Environmental Sciences and Engineering, Peking University, Beijing 100871, China

⋆These authors contributed equally to this work.

Correspondence to: Jianzhong Xu (jzxu@lzb.ac.cn)

https://doi.org/10.5194/essd-2022-211
Preprint. Discussion started: 4 July 2022

Abstract

Atmospheric aerosol in the Tibetan Plateau (TP) and its surroundings has received widely scientific concern in recent decades owing to its significant impacts on regional climatic and cryospheric changes, ecological and environmental securities, and hydrological cycle. However, our understanding on the atmospheric aerosol in this remote region is highly limited by the scarcely available dataset, which has been proved to be an important factor on disturbing the climate and environment in this region. The extremely harsh natural conditions hamper the exploration of the observation. This condition has been improved in recent decade by constructing a few stable field observatories at typical sites on the TP and its surroundings. A comprehensive project was carried out since 2015 to investigate the properties and sources of atmospheric aerosols as well as their regional differences in the vast TP regions by performing multiple short-term intensive field observations using a suite of high-resolution online instruments. This paper presents a systematic dataset of the high-time-resolution (hourly scales) aerosol physicochemical and optical properties at seven different sites over the TP and its surroundings from the observation project, including the size-resolved chemical compositions of submicron aerosols, standard high-resolution mass spectra and sources of organic aerosols, size distributions of particle number concentrations, particle light scattering and absorption coefficients, particle light absorptions from different carbonaceous substances of black carbon and brown carbon, number concentrations of cloud condensation nuclei, and concentrations of gaseous pollutants. In brief, atmospheric aerosols in these remote sites were all well-mixed and highly-aged due to their regional transport sources. However, high contributions of carbonaceous organic aerosols, overall neutralized submicron aerosols, and relatively higher light absorption capability were observed in the southern TP, whereas secondary inorganic species contributed dominantly to the overall acidic submicron aerosols in the northern TP. In addition to the insights into the regional differences of aerosol sources and properties in the vast TP regions, the datasets are also useful for the simulation of aerosol radiative forcing and the evaluation of interactions among different components of the Earth system in numerical models. The datasets are available from the National Cryosphere Desert Data Center, Chinese Academy of Sciences (https://doi.org/10.12072/ncdc.NIEER.db2200.2022; Xu, 2022).

https://doi.org/10.5194/essd-2022-211
Preprint. Discussion started: 4 July 2022

1 Introduction

Tibetan Plateau (TP), with a mean altitude of over 4000 m a.s.l. and a huge surface area of approximately 2.5×10^6 km^2, is the highest and largest plateau on the Earth. The mountain ranges on the TP and its surroundings are one of the most important cryospheric regions in the world. Therefore, the TP has been widely known as the "roof of the world", the "Third Pole", and the "Asian Water Tower" (Qiu, 2008; Yao et al., 2019). The TP and its surroundings have exerted significant roles in the global and regional climate systems, hydrological cycles, and cryospheric changes through its huge and complex topography and heat source (Duan and Wu, 2005; Yao et al., 2012; Chen et al., 2021). Over the past few decades, more concerns have been raised in the TP and its surroundings due to the significant climatic warming and rapid cryospheric changes in this region (Kang et al., 2010). For example, TP has shown significant warming during the last half century and will warming more rapidly than the global average in the future (You et al., 2021; Zhou and Zhang, 2021).

As the most complex and important component in the atmosphere, atmospheric aerosols play significant roles in the climatic and cryospheric changes in the TP regions through their crucial direct and indirect effects on solar radiation and the albedos of snow/ice surfaces (Xu et al., 2009; Kang et al., 2019b; Zhang et al., 2020a; Yang et al., 2021). Atmospheric aerosols, particularly the two important light-absorbing carbonaceous substances of black carbon (BC) and brown carbon (BrC), can absorb the solar radiation directly, warm the atmosphere, and finally lead to a positive forcing on Earth's energy budget (Ramanathan et al., 2007; Kopacz et al., 2011; Laskin et al., 2015). In addition, aerosol particles over the TP also exert significant impacts on ice cloud properties and the vertical motions of the atmosphere and cloud development through their semi-direct effects (Liu et al., 2019). Since the direct observation of atmospheric aerosols over the TP region is remarkably difficult due to its harsh environment, the numerical model simulation based on reanalysis data has become the most popular research approach over the past decades. Lau et al. (2006) evaluated the significant impact of atmospheric aerosols over the TP on the intensification of the Asian summer monsoon by using the NASA finite-volume general circulation model. Kopacz et al. (2011) investigated the origin and radiative forcing of BC transported to the TP and Himalayas by using the GEOS-Chem global chemical transport model, while He et al. (2014) evaluated the model simulations of BC over the TP by a global 3-D GEOS-Chem chemical transport

https://doi.org/10.5194/essd-2022-211
Preprint. Discussion started: 4 July 2022

model. Ji et al. (2015) simulated the distribution, deposition, transportation, and climatic effects of carbonaceous aerosols over the TP regions by using a regional climate model coupled with a chemistry–aerosol module. Liu et al. (2015) investigated the transport of summer dust and anthropogenic aerosols over the TP by using a three-dimensional aerosol transport–radiation model and found heavily loaded dust aerosols over the northern slope of the TP while anthropogenic aerosols over the southern slope. Zhang et al. (2017) applied a regional chemistry and transport model to study the significant trans-Himalaya transport of aerosol pollutants from India and nearby regions to the inland TP region. Ma et al. (2019) modelled the emissions, chemistry, and transport of aerosols and their precursors in the tropopause over the TP during the Asian summer monsoon by using the ECHAM/MESSy Atmospheric Chemistry (EMAC) general circulation model. Although important findings have been reported from those model simulations, the in-situ observation of atmospheric aerosols over the TP regions has become more crucial and urgent due to their key roles in evaluating and improving the model performances over the remote region.

Numerous in-situ measurements have been conducted in the TP and its surroundings during the past few years to characterize the aerosol properties, sources, transport pathways, and regional distributions through the filter sample collection of atmospheric aerosol and the aerosol depositions in glaciers, snow cover, precipitation, and lake sediment (Kang et al., 2022). The off-line atmospheric filter sampling was one of the most important and popular in-situ aerosol collection method in the TP because it was relatively low-cost and easy to carry out under the extreme harsh natural conditions and difficult logistical supports (Cao et al., 2009; Zhao et al., 2013; Xu et al., 2014a; Zhang et al., 2014; Cong et al., 2015; Wan et al., 2015; Xu et al., 2015; Kang et al., 2016; Li et al., 2016b; Dong et al., 2017; Xu et al., 2020). Meantime, characterizing the regional distribution of atmospheric aerosols over a large area of the TP was another important advantage of the off-line filter sampling through their simultaneous observations at multiple sites (Li et al., 2016a; Chen et al., 2019; Kang et al., 2022). However, studies on the atmospheric aerosols over the remote TP regions are still insufficient at present. The observational data was generally scattered and unsystematic with relatively few data points because most of these in-situ observations in this region were carried out at single site aiming to investigate few aerosol properties with relatively low temporal resolution (from days to weeks) during different individual campaign. Up to now,

https://doi.org/10.5194/essd-2022-211
Preprint. Discussion started: 4 July 2022

comprehensive researches focusing on multiple aerosol physicochemical and optical properties through the real-time online consecutive measurements (high temporal resolutions of minute to hour scale) at multiple sites are still rare in the TP.

Studies about the atmospheric aerosols, especially the aerosol chemistry, have achieved great progress during the last decade in China due to its serious haze pollution problems. The Aerodyne high-resolution time-of-flight aerosol mass spectrometer (HR-ToF-AMS) was one of the most popular online instrument that successfully implemented in numerous aerosol chemistry observations to characterize the real-time size-resolved chemical compositions and sources of submicron aerosols (Li et al., 2017; Zhou et al., 2020). However, study of the aerosol chemistry using such online instruments was still scarce in the TP regions due to the extremely harsh observation conditions. Since 2015, a comprehensive and systematic observation project, aiming to investigate the regional differences on the aerosol sources and physicochemical and optical properties in the different TP regions, has been launched by our research team by performing the high-resolution real-time online measurements at different sites in the TP and its surroundings during almost every year. This paper serves to describe in detail the high-resolution dataset about the physicochemical and optical properties of atmospheric aerosols over the TP and its surroundings from the project. Descriptions of the observation sites, instrumental deployments, and data processing methods are introduced in Sects. 2 and 3, while the high-time-resolution (hourly scale) data of aerosol physical, chemical, and optical properties are discussed in detail in Sect. 4. This datasets provide not only comprehensive data for the understanding of regional differences in aerosol sources and properties in different TP regions, but also basic inputs for the simulation of aerosol radiative forcing and the assessments of interactions among different components of the Earth system in future models.

2 Observation site descriptions

The comprehensive observations of atmospheric aerosol chemistry were conducted at seven different sites in the different regions of TP and its surroundings in recent years. All the sites include six remote sites and one urban site which is used for comparison. Figure 1 illustrates the geographical locations of these sites and the picture of each observation. Table 1 provides detailed information about the full name and geographic characteristics (latitude, longitude, and altitude) of each site as well as the sampling period and available instruments during each field campaign. The following text gives

https://doi.org/10.5194/essd-2022-211
Preprint. Discussion started: 4 July 2022

a brief description of each site.

2.1 QOMS

The Qomolangma Station for Atmospheric and Environmental Observation and Research, Chinese Academy of Sciences (QOMS for short in this study and similarly hereinafter for other sites; 86.56ºE, 28.21ºN; 4276 m a.s.l) is situated in the basin of Rongbuk valley, the northern slope of Mt. Everest (~30 km away). The station is about 80 km away from the Tingri county and 650 km away from the Lhasa city. The climate in the northern slope of Mt. Everest has obvious seasonal variation due to the Indian monsoon transition characteristics. During the pre-monsoon season (dry period), the dominated westerly and southerly winds play important roles in the long-range transport of atmospheric pollutions from the South Asia, whereas the southwesterly winds prevail during the monsoon season and bring warm and wet airflow from the Indian Ocean to this region with increasing humidity and precipitation. The QOMS is an important and ideal high-altitude observatory at the south edge of the TP for studying the transboundary transport of atmospheric pollutants from South Asia to the TP.

2.2 Motuo

The Motuo county, with an area of ~34,000 km^2 and a population of ~15,000, is situated in the lower reaches of the Yarlung Tsangpo River and the southern slope of the eastern Himalayas and Gangrigab Mountains, in the southeast edge of the TP. The terrain in the whole area of the Motuo county is high in the north and low in the south, ranging from 200 to 7787 m with an average altitude of ~1200 m. The huge altitude difference makes the Motuo county has the most complete vertical climatic zones in China, e.g., tropical, subtropical, and alpine cold zones. The county seat of Motuo (29.30°N, 95.32°E; 1305 m a.s.l) is located at a halfway up a mountain and has a subtropical humid climate with relatively high temperature and abundant rainfall. The annual precipitation can reach 2358 mm in Motuo county with relative humidity more than 80%. Due to the minor population and extremely scarce industrial activities, Motuo county is also a relatively pristine region in the TP. Moreover, the sampling site in Motuo is set at the summit of a hill that towards to the Yarlung Tsangpo grand canyon, which makes it a very ideal site in the southeast edge of the TP to directly monitor the transboundary transport of atmospheric pollutants and moisture from Southeast Asia and Indian Ocean to the TP.

2.3 NamCo

https://doi.org/10.5194/essd-2022-211
Preprint. Discussion started: 4 July 2022

The Nam Co Station for Multisphere Observation and Research, Chinese Academy of Sciences (NamCo; 90.95ºE, 30.77ºN; 4730 m a.s.l) is a high-altitude observatory at the central part of the TP. This station is situated at the southeast shore of Nam Co Lake. The surrounding of this station is a pristine region in the TP and isolated from major industrial sources and populated areas. The station is ~60 km to the west away from the closest town (Damxung) and ~125 km to the northwest away from the Lhasa, the capital city of the Tibet Autonomous Region, China. The region is generally affected by the typical semi-arid plateau monsoon climate with more precipitation during the summer monsoon season. The NamCo is the most important site in inland of the TP and dominated by air mass from south and west.

2.4 Waliguan

The China Global Atmospheric Watch Baseline Observatory, Mount Waliguan Base (Waliguan; 100.9ºE, 36.28ºN; 3816 m a.s.l) is situated at the top of the Mt. Waliguan (mountain height of ~600 m). The observatory is one of the twenty-nine baseline stations of Global Atmosphere Watch (GAW) of the World Meteorological Organization (WMO) and has become an important platform for monitoring the global background conditions of atmospheric environment and chemistry since 1994. The Mt. Waliguan is situated ~30 km to the east of the Gonghe county and ~90 km to the southwest away from the capital city (Xining) of Qinghai Province, China. The Mt. Waliguan is also a relatively pristine region with little influence from human activities. The Waliguan is an important observatory in the northeast edge of the TP and dominated by air mass from northeast during the summer season, which makes it an ideal site to study the influence of air pollutants from the industrial areas in the northwestern China to the TP.

2.5 LHG

The Qilian Observation and Research Station of Cryosphere and Ecologic Environment, Chinese Academy of Sciences (39.50°N, 96.51°E; 4180 m a.s.l) is built near the terminus (~1 km) of the Laohugou Glacier No.12. This glacier is the largest valley glacier in the Laohugou glacier group that situated on the northern slope of the western Qilian Mountains in the northeast part of the TP. Therefore, this station is referred to as LHG for short in this study. The climate in this region is a typically arid and continental climate and dominated by the East-Asian monsoon in the summer and Westerlies in the

https://doi.org/10.5194/essd-2022-211
Preprint. Discussion started: 4 July 2022

winter. The precipitation is mainly occurred from May to September, accounting for 65−80% of the whole year. The closest major village is located ~60 km to the northwest with a population of ~1000 while the closest city (Yumen) is approximately 100 km to the north of the station with a population of ~140,000. Overall, the LHG is another representative station in the northeastern TP and significantly isolated from the human living areas, and therefore, is also well suited for sampling the background air mass and studying the transport mechanisms and potential impacts of air pollutants from its surrounding regions.

2.6 Bayanbulak

The Bayanbulak National Basic Meteorological Station (Bayanbulak; 84.35° N, 42.83° E; 2454 m a.s.l) is located in the Bayanbulak grassland at the northwest of Hejing county, Bayingol Mongolian Autonomous Prefecture, Xinjiang Uygur Autonomous Region, China, which is the boundary area of the northern and southern Xinjiang. The grassland is situated in an intermontane basin in the central Tianshan Mountains and surrounded by numerous snow mountains with altitudes more than 3000 m. The Bayanbulak grassland is a typical mountain meadow grassland and one of the most important animal husbandry bases in Xinjiang. In addition, the Bayanbulak grassland is also an ideal breeding habitat for wild animals due to the minor influence from anthropogenic activities. The climate in Bayanbulak grassland belongs to the typical temperate continental mountain climate with annual average precipitation of ~200−300 mm. The Bayanbulak town is approximately 300 km away from the Korla city, the second largest city in Xinjiang. The town has limited human activities and traffic transportation. Therefore, this site is also a typical remote site for monitoring the background condition of atmospheric aerosols.

2.7 Lhasa

Lhasa (29.65°N, 91.03°E; 3650 m a.s.l) is the capital city of the Tibet Autonomous Region, China that located in the south-central part of the TP. The city lies in a flat river valley with the surrounding mountains reaching 5500 m a.s.l. and the Lhasa River passing through the city from west to east. Lhasa has a continental monsoon climate with dry and frosty winter but wet and warm summer. Affected by the high altitude and the dominant downdraft, Lhasa has sunny weather all year round and therefore has been called as the “sunlit city” due to the strong solar radiation. The observation site in Lhasa

https://doi.org/10.5194/essd-2022-211
Preprint. Discussion started: 4 July 2022

is located in the Binhe Park near the Lhasa River. The Norbulingka scenic area, one of the main activity center for local Tibetans to celebrate their religious festivals (e.g., the Sho Dun festival), is located ~1 km to the northwest of the sampling site, while the Potala Palace, the center of Tibetan Buddhism, is ~1.8 km to the northeast. Besides, the Jinzhu East Road, an arterial road in Lhasa with relatively large traffic flow is only 100 m away from the north of the site. Since the unique energy structure and different residential habit in Lhasa comparing with those remote sites, a comparative observation is conducted in this urban site for studying the primary aerosol properties and sources from various residential combustion activities.

3 Online sampling, instrumental setup, and data processing

3.1 Online real-time aerosol sampling over the TP

The online-based observation of atmospheric aerosols was carried out using a series of real-time high-resolution instruments at each site, usually including a HR-ToF-AMS (Aerodyne Research Inc., Billerica, MA, USA) for acquiring the chemical compositions (organic aerosol (OA), nitrate, sulfate, ammonium, and chloride) of non-refractory submicron aerosol (PM_1), a scanning mobility particle sizer (SMPS, model 3936, TSI Inc., Shoreview, MN, USA) for acquiring the size distribution of number concentration of submicron particles, a photoacoustic extinctiometer (PAX, DMT Inc., Boulder, CO, USA) for acquiring the particle light absorption, scattering, and extinction coefficients (B_{abs}, B_{scat}, and B_{ext}) and single scattering albedo (SSA) at 405 nm as well as the mass concentration of BC, an Aethalometer (model AE33/AE31, Magee Scientific Corp., Berkeley, CA, USA) for acquiring the B_{abs} at seven fixed wavelengths (i.e., 370, 470, 520, 590, 660, 880, and 950 nm), and a cloud condensation nuclei (CCN) counter (model CCN-100, DMT Inc., Boulder, CO, USA) for acquiring the CCN number concentration at different supersaturation (*SS*) of water vapor. In addition, the concentrations of gaseous pollutants including the carbon monoxide (CO), ozone (O_3), sulfur dioxide (SO_2), nitric oxide (NO), nitrogen dioxide (NO_2), and nitrogen oxides (NO_X) were measured using a suite of gas analyzers (models EC9830/9850/9810/9841, Acoem Ecotech Inc., Knoxfield, VIC, Australia), whereas the concentration of carbon dioxide (CO_2) was acquired by a CO_2 sensor (model 840A, LI-COR Inc., Lincoln, NE, USA). The specific instrumental deployment and sampling period during each observation campaign is summarized in Table 1.

As the core instrument for the observation of atmospheric aerosol chemistry in this

https://doi.org/10.5194/essd-2022-211
Preprint. Discussion started: 4 July 2022

study, HR-ToF-AMS was deployed during all the campaigns, while SMPS at QOMS, Motuo, LHG, and Lhasa, PAX at QOMS, Motuo, Waliguan, and Lhasa, Aethalometer at QOMS, NamCo, and Waliguan, CNN-100 at Motuo and Waliguan, and Gas analyzers at Motuo and Lhasa, respectively. The observations in the central or southern TP regions were mainly conducted during the pre-monsoon periods, such as 12 April to 12 May at QOMS, 26 March to 22 May at Motuo, and 31 May to 1 July at NamCo, aiming to study the transboundary transport of atmospheric pollutants from those polluted regions in South Asia to the inland of the TP. Whereas measurements in those remote regions in the northern TP and its surroundings were performed during summer, i.e., 1 to 31 July at Waliguan, 4 to 29 August at LHG, and 29 August to 26 September at Bayanbulak, respectively, for monitoring the aerosols transported from the surrounding polluted regions under the enhanced East Asian monsoon. The observation at Lhasa was conducted between 31 August and 26 September in consideration of the strongest atmospheric oxidation capability during the summer.

3.2 Instrumental setup

In spite of the observation instruments are somewhat different during each campaign, the instrumental sampling settings are generally similar. Figure 1b shows the basic sampling setup of instruments during the online aerosol observations. All instruments were generally placed in an air-conditioned room or trailer. The indoor temperature was generally maintained at ~18℃ to ensure the observation performance of instruments and vacuum pumps. The ambient aerosols were firstly sampled into a fine particle cyclone (model URG-2000-30EH, URG Corp., Chapel Hill, NC, USA) to remove those particles with aerodynamic diameter (D_{va}) above 2.5 μm. Then, fine particles were introduced into a diffusion silica gel dryer or a Nafion dryer through 0.5-inch stainless steel tubes to dry the airflows. Finally, particles were sampled into a series of online instruments for the real-time measurements. In order to match a good efficiency in size cut for the fine particle cyclone, an external vacuum pump was also equipped in the sampling system for discharging the excess sampling flow. Detailed description of the instrumental setups can be found in previous publications (Xu et al., 2018; Zhang et al., 2018; Zhang et al., 2019; Zhao et al., 2022).

3.3 Instrumental operation and data processing

3.3.1 HR-ToF-AMS operation

https://doi.org/10.5194/essd-2022-211
Preprint. Discussion started: 4 July 2022

The HR-ToF-AMS is one of the most advanced instruments that widely used for the study of atmospheric aerosol chemistry worldwide. The detailed principle of HR-ToF-AMS can be obtained elsewhere (DeCarlo et al., 2006). The HR-ToF-AMS is mainly composed by three different sections that separated by small apertures and differentially pumped, i.e., a particle beam generation section to form a concentrated and narrow particle beam through a critical orifice and a six-stage aerodynamic lens, a particle-sizing chamber to measure the particle aerodynamic sizes through a particle time-of-flight measurement (different velocities and arrival times for size-dependent particles in a known flight distance), and a particle chemical composition detection section to directly vaporize the particle beam at a ~600 °C resistively heated surface, ionize the particles into positively charged ion fragments by a 70 eV electron impact, and then detect their chemical composition by a high-resolution mass spectrometer (Jimenez et al., 2003). There are two different operation modes in HR-ToF-AMS, i.e., V-mode (detection limits of about 10 ng m^{-3}) and W-mode (~5000 m/Δm) with different signal-to-noise ratio (S/N). However, the HR-ToF-AMSs were only operated at the V-mode during almost all the seven field campaigns in consideration of the relatively low aerosol mass concentration level and low S/N ratio over the TP. The mass concentration and size distribution of non-refractory PM_1 chemical species were obtained by further switching the instrument between mass spectrum (MS) mode and particle time-of-flight (PToF) mode every 15s under the V-mode operation. However, there are no observation of particle sizes during the NamCo and LHG measurements due to the malfunction of the chopper. In addition, the HR-ToF-AMS need to be calibrated for its flow, ionization efficiency (IE), and sizes at the beginning and end of each observation (Jayne et al., 2000). The relative IE (RIE) of ammonium and sulfate were calibrated using the mono-dispersed pure ammonium nitrate and ammonium sulfate particles, respectively, with the selected sizes of 200–300 nm, while the particle size was calibrated using the mono-dispersed ammonium nitrate particles with sizes varied from 60 to 600 nm. Finally, default RIE values were assumed to be 1.1, 1.3, and 1.4 for nitrate, chloride, and OA, respectively, during all the field campaigns, while different RIE values were set for ammonium and sulfate according to their calibration results during each campaign, e.g., 3.9 and 4.2 for ammonium and 1.6 and 1.4 for sulfate based on two calibrations in the QOMS measurement.

3.3.2 HR-ToF-AMS data processing

https://doi.org/10.5194/essd-2022-211
Preprint. Discussion started: 4 July 2022

The HR-ToF-AMS data was processed using the standard data analysis software with SQUIRREL and PIKA toolkits written in Igor Pro (Wavemetrics Inc., Lake Oswego, OR, USA). The SQUIRREL used a fragmentation table to apportion the measured signals at each mass-to-charge ratio (*m*/*z*) into different species to quantify the chemical composition of non-refractory PM_1 species, while the PIKA employed a modified Gaussian fitting algorithm to obtain the ion-speciated high-resolution mass spectra (HRMS) and elemental composition of OA (Allan et al., 2004; DeCarlo et al., 2006). The elemental ratios of OA, i.e., oxygen-to-carbon (O/C), hydrogen-to-carbon (H/C), organic matter-to-organic carbon (OM/OC), and nitrogen-to-carbon (N/C), were determined using the improved method (Canagaratna et al., 2015) during all the seven observation campaigns. In addition, a collection efficiency (CE) was generally introduced to compensate for the incomplete transmission and detection of particles through the aerodynamic lens and bouncing at the vaporizer surface in most AMS studies. Previous study has revealed that the CE is significantly influenced by the relative humidity (RH) in sampling line and the acidity and ammonium nitrate mass fraction (ANMF) in the sampled aerosols, which has been concluded as a build-in composition-dependent CE (CDCE) algorithm in the standard data processing software (Middlebrook et al., 2012). Generally, a high RH, a high aerosol acidity, or a high ANMF often corresponds to a high CE value. However, the RH in the sampling system is always maintained below 40% due to the professional deployments of dryers in the front of the sampling system and the ANMF is basically below 0.4 due to the low contributions of nitrate and ammonium during all the seven observation campaigns (see Sect. 4.1 for detail), which means the negligible effects of these two parameters on CE in our study. Therefore, default CE value of 0.5 were finally employed during the QOMS, NamCo, Waliguan, and Lhasa campaigns in consideration of their overall neutralized or slightly acidic aerosols, whereas the CDCE values were adopted at Motuo, LHG, and Bayanbulak where bulk submicron aerosols were acidic (see Sect. 4.2 for detail).

3.3.3 OA source apportionment using PMF analysis

Source apportionment of OA during each observation was conducted by the positive matrix factorization (PMF) analysis on organic matrix data using the PMF2.exe algorithm in robust mode (Paatero and Tapper, 1994) and the standard PMF Evaluation Tool (PET, Ulbrich et al., 2009) written in Igor Pro software. The PMF analysis was

https://doi.org/10.5194/essd-2022-211
Preprint. Discussion started: 4 July 2022

evaluated thoroughly according to the standard procedures outlined in Zhang et al. (2011) by down-weighting, modifying, or removing some ion fragments in the data and error matrices. Firstly, those ions at *m*/*z* >120 and all the isotope ions were generally excluded because of the insufficient ability to resolve the deconvolution due to their low signals. Then, the signals of the four organic ions of O^+, HO^+, H_2O^+, and CO^+ were scaled to that of CO_2^+ according to the suggested fragmentation table in Aiken et al. (2008) and further down-weighted in PMF analysis. Thirdly, all those "bad" ions (S/N <0.2) were removed from the data matrices, while all the "weak" ions (0.2< S/N <2) were downweighted by increasing their errors. In addition, some runs and some ions which had obviously huge residual spikes were also removed in order to avoid their unnecessary interference. After the above pre-processing, the PMF solutions were investigated by selecting a certain variation range of factor number and rotational parameter (*f*Peak), e.g., 1−6 factors with *f*Peak varying from –1 to 1. Finally, the optimal solution of PMF analysis were determined after a comprehensive evaluation by examining the model residuals at each *m*/*z* and each time, comparing the factor mass spectrum with corresponding reference spectrum, comparing the temporal variation of individual factor with external tracers, and analyzing the diurnal variation pattern of each factor. Totally, 2-, 3-, or 4-factor solution were selected during the different field campaigns in this study as discussed in Sect. 4.6.

3.3.4 Operation and data processing of other instruments

The operation principles and data processing methods of other online instruments are described briefly as follows. The SMPS is composed by an electrostatic classifier (EC, model 3080) equipped with a long-differential mobility analyzer (long-DMA, model 3081) and a condensed particle counter (CPC, model 3772). Ambient particles are measured through an electrical mobility detection technique in this instrument, e.g., a bipolar charger in the EC is utilized to charge the particles to a known charge distribution, then classify them according to their ability to traverse an electrical field in the long-DMA, and finally count those screened monodisperse particles by the CPC. The sample and sheath flow rates are 0.3 and 3.0 L min^{-1}, respectively, at both QOMS and Lhasa which measure particles between 14.6 and 661.2 nm in mobility diameter (D_m), whereas the sample and sheath flow rates are 0.5 and 5.0 L min^{-1} at LHG and Motuo and sample particles at a size range of 10.9−495.8 nm in D_m. The number concentrations of submicron particles in 107 different size channels are firstly recorded

https://doi.org/10.5194/essd-2022-211
Preprint. Discussion started: 4 July 2022

at an initial time resolution of 5 min and then converted to the total number and volume concentrations according to the obtained size distribution of number concentration. The PAX directly measures the B_{abs} and B_{scat} of aerosol particles at 405 nm by using a modulated diode laser, namely measures the B_{abs} by an in-situ photoacoustic technique while the B_{scat} using a wide-angle integrating reciprocal nephelometer. The B_{ext} is the sum of B_{abs} and B_{scat} while the SSA is calculated as the ratio of B_{scat} to B_{ext}. The BC mass concentration is calculated as the ratio of measured B_{abs} to a fixed BC mass absorption cross-section (MAC) value of 10.19 m^2g^{-1} at 405 nm. In addition, the B_{scat} is calibrated using the high-concentration ammonium sulfate particles generated by the aerosol generator, while the B_{abs} is calibrated using the sufficient black smoke from a kerosene lamp before each field campaign according to the operator manual of this instrument. The Aethalometer is used to measure the particle B_{abs} at seven wavelengths (370−950 nm), which firstly measures the light attenuation between particle-laden and particle-free sample spots on the filter and finally converts the attenuation to particle B_{abs} in ambient air. The filter-based loading effect and multiple scattering effect are corrected during all the three observations to eliminate the difference between the light attenuation measured at the filter and the ambient particle B_{abs}. The absorption Ångström exponents (AAE) value is acquired through a power-law fitting of B_{abs} following the typical Beer-Lambert's law, i.e., $\mathrm{AAE} = ln\,(B_{abs,\lambda 1}/B_{abs,\lambda 2})/ln(\lambda_2/\lambda_1)$. Furthermore, a traditional AAE method was adopted to quantitatively apportion the total B_{abs} into two parts from BC and BrC ($B_{abs,BC}$ and $B_{abs,BrC}$) at 370−660 nm during each campaign. The contribution of BrC to total B_{abs} ($fB_{abs,BrC}$) at a short wavelength λ is calculated as $fB_{abs,BrC,\lambda} = 1 - (B_{abs,880}/B_{abs,\lambda}) \times (\lambda/880)^{-\mathrm{AAE_{BC}}}$ by assuming its negligible contribution at 880 nm. Detailed information about the data correction and calculation of this instrument can be found in our previous publication (Zhang et al., 2021). The CCN-100 supersaturates the sampled aerosol particles in a 50-cm-high column with continuously wetted walls and a longitudinal thermal gradient, so that those particles grow into detectable CCN particles and are measured using an optical particle counter among 20 different size bins. The number concentrations of CCN are measured consecutively at five different *SS* values of 0.2%, 0.4%, 0.6%, 0.8%, and 1.0%. The CCN data is recorded every 5 minutes at each *SS* and finally has a time resolution of 30 minutes during a complete measurement cycle. The concentrations of gaseous pollutants are measured using four familiar Ecotech-series gas analyzers and a

https://doi.org/10.5194/essd-2022-211
Preprint. Discussion started: 4 July 2022

LI-COR CO_2 sensor. All the instruments are calibrated for their zero and span points using the Zero Air Generator and the high-precision standard gases, respectively, before each observation. The concentrations are generally recorded at 1 second resolutions and finally convert to hourly scales in this study.

4 Aerosol physicochemical and optical properties over the TP

4.1 Aerosol loading and chemical compositions of submicron aerosols

An overview of the high-time-resolution temporal variations of PM_1 chemical species (OA, nitrate, sulfate, ammonium, chloride, and BC) during the seven observations in the TP and its surroundings is shown in Fig. 2. Normally, mass concentrations of PM_1 and its chemical species varied dynamically, with high mass loading period and low mass loading period appeared alternatively throughout the sampling period of each campaign. Although the sampling years (2015−2021), seasons (March−September), and altitudes (1350−4730 m a.s.l.) of these sites were different, the significantly distinct PM_1 mass and chemical compositions could basically reflect the regional difference of aerosol mass levels, properties, and sources at different regions. On average, the mass concentration of total PM_1 among the seven campaigns ranged from 1.9 to 9.1 μg m^{-3} (Fig. 3 and Table 2). The maximum PM_1 mass was observed at Waliguan due to the transport of industrial aerosols and gaseous pollutants from those urban areas in northwestern China, whereas the minimum value was measured at Bayanbulak due to its background condition. The average PM_1 mass level in the TP and its surroundings was comparable to the values observed at various high-altitude, coastal, forest, and remote background sites worldwide (0.46−15.1 μg m^{-3}; Table 3), but was significantly lower than those observed at abundant urban (34.4−71.5 μg m^{-3}) and suburban (21.4−44.9 μg m^{-3}) sites in other regions of China (Li et al., 2017), suggesting the essentially clean nature of atmosphere condition in the Third Pole region.

More importantly, the chemical compositions of PM_1 showed significantly regional difference (Fig. 3), hinting the distinct aerosol sources at different TP regions. OA and BC, the two dominant components from biomass burning activities (Bond et al., 2004), together contributed more than 69.1−85.7% of the total PM_1 mass at the four sites of QOMS, Motuo, NamCo, and Lhasa in the southern or central TP (Table 2). These high contributions were mainly attributed to the frequent transport of biomass-burning-related emissions from those polluted regions in South and Southeast Asia to the remote sites of TP during the pre-monsoon season (Bonasoni et al., 2010; Cong et al., 2015;

https://doi.org/10.5194/essd-2022-211
Preprint. Discussion started: 4 July 2022

Zhang et al., 2018) or the intense local biomass burning activities in the Lhasa site (Cui et al., 2018; Zhao et al., 2022). On the contrary, contributions of the three inorganic species (i.e., sulfate, nitrate, and ammonium; SNA) to total PM_1 were more than 60% at the three northern sites of Waliguan, LHG, and Bayanbulak. The most dominant contributions of SNA species were from the sulfate (38.1−46.0%), which were consistent with the results observed at another high-altitude site in the northeastern TP (Menyuan; 28%) and other rural and remote sites (19–64%) in East Asia due to the regional transported sources (Du et al., 2015). The high contributions of SNA, particularly the sulfate, in the northern TP and its surroundings were mainly related to the regional transport of anthropogenic aerosols and gaseous precursor emissions from those industrial urban areas in the northwest of China and the possibly important in-cloud aqueous reactions at the mountains (Zhang et al., 2019).

4.2 The bulk acidity of submicron aerosols

Particle phase acidity is an important parameter of aerosol physicochemical properties, which have significant impacts on the hygroscopic growth, toxicity, and heterogeneous reactions of aerosol particles, however, is still difficult to be determined directly using the online measurement. Bulk acidity of submicron aerosols from the Aerodyne AMS measurement was generally evaluated following the methods in Zhang et al. (2007b) and Schueneman et al. (2021). The mass concentration of ammonium was firstly predicted by assuming to fully neutralize these measured sulfate, nitrate, and chloride, i.e., $NH_{4\,Predicted}^{+} = 18 \times (2\times SO_4^{2-}/96 + NO_3^{-}/62 + Cl^{-}/35.5)$. The mass concentration ratio of measured ammonium to predicted ammonium ($NH_{4\,Measured}^{+}/NH_{4\,Predicted}^{+}$) was further calculated to be a good indicator to evaluate the bulk acidity of submicron aerosols. Aerosol particles are generally considered to be "acidic" if the calculated ratio is lower than 1 and to be "more acidic" if the ratio is lower than 0.75, whereas a ratio that roughly near to 1 or larger than 1 indicates the particles are "bulk neutralized" and even there are more excess ammonium that needed to be neutralized. Note that the validity of using this method is based on the assumption that the influence from nitrogen- or sulfur-containing organic ions (e.g., organic acids and organic nitrogen compounds) as well as the mineral and metal ions are negligible (Zhang et al., 2007b).

The bulk acidity of submicron aerosols in the different TP regions was evaluated by performing the linear regression analysis between the mass concentrations of measured and predicted ammonium during the seven campaigns (Fig. 4). Obviously, bulk acidity

https://doi.org/10.5194/essd-2022-211
Preprint. Discussion started: 4 July 2022

of submicron aerosols showed obviously regional difference between the southern and northern TP regions, mainly attributed to their different aerosol sources. The regression slopes were fitted to be 1.2, 1.11, and 1.18 at the three sites of QOMS, NamCo, and Lhasa that located in the southern or central TP, indicating the submicron aerosol particles at the three sites were generally neutralized and even excesses of ammonium. The result was consistent with the previous finding that high availability of ammonia were monitored from agriculture emissions in the South Asia (Van Damme et al., 2015). In addition, as the findings in our previous publications, atmospheric aerosols at QOMS and NamCo were significantly influenced by the transport of biomass-burning-related emissions from South and Southeast Asia during the pre-monsoon season (Xu et al., 2018; Zhang et al., 2018), while various biomass fuels were burned intensely during those frequent religious festivals in the Lhasa urban areas (Zhao et al., 2022). Differently, the submicron particles were overall acidic with regression slopes between 0.73 and 0.86 at the rest four sites, especially in the two northern TP sites (LHG and Bayanbulak) where sulfate contributed significantly to total PM_1 (46.0% and 41.6%). Similar acidic submicron aerosol particles have also been observed at Menyuan and LHG in the northern TP in previous studies (Du et al., 2015; Xu et al., 2015), mainly related to the transport of the enriched SNA species or their gaseous precursors from the industrial areas in northwestern China to the remote regions in the northern TP.

4.3 Size distribution of PM_1 chemical species

The size distributions of non-refractory PM_1 chemical species were analyzed through the PToF measurement in HR-ToF-AMS, which were helpful for the understanding of aerosol sources, oxidation degrees, mixing states, formation, transformation, and growth mechanisms as well as their impacts on the CCN activity. Normally, size distributions were peaked at accumulation mode (e.g., ~400−600 nm in D_{va}) for those SNA species and oxidized OA components as a result of their secondary formation, whereas fresh organics from primary emission sources like traffic exhausts, cooking, and coal combustion generally had an additional mass distribution shifting to smaller sizes (Zhang et al., 2005b; Aiken et al., 2009). Considering the overall dominant mass contributions and complex atmospheric sources, only organics was selected to demonstrate the regional difference in size distribution in the different TP regions in this study. As shown in Fig. 5a and Table 2, the peak diameters in the size distribution of OA mass concentrations varied significantly from 510 nm at QOMS to a smaller size

https://doi.org/10.5194/essd-2022-211
Preprint. Discussion started: 4 July 2022

of 228 nm at Lhasa, suggesting the distinctly different sources and aging processes of atmospheric aerosols in different TP regions. For example, OA has been reported to be internally well-mixed and aged at QOMS due to the long-range transport aerosol sources of biomass-burning-related emissions from South Asia, whereas local primary sources including cooking, traffic exhausts, and biomass burning together contributed more than 60% of the total OA at the urban site in Lhasa (Zhang et al., 2018; Zhao et al., 2022). The crucial influence of aerosol sources to size distributions has further been confirmed quantitively in Fig. 5a where the peak diameters in OA size distributions correlated tightly (R^2 = 0.92) with the O/C ratios of OA.

4.4 Diurnal variation of PM_1 chemical species

Diurnal variations of PM_1 chemical compositions are usually influenced by multiple factors, including the variations in meteorological conditions (e.g., planetary boundary layer (PBL) height, wind direction and speed, temperature, RH, etc.), different primary emission sources (e.g., intense vehicle exhausts during traffic rush hours, cooking emissions, and coal combustion emissions from heating activities), and distinct formation mechanisms (e.g., daytime photochemical oxidation processes, nighttime heterogeneous reactions, and gas-particle partitioning of secondary species). Therefore, a comprehensive understanding of the diurnal variation characteristics of different aerosol chemical compositions is not only beneficial to investigate of their dynamic evolution processes but also helpful to understand the key factors (source, meteorology, or secondary formation) that dominated the variations of different chemical species. Obviously, different diurnal variation patterns of the total PM_1 mass concentrations were observed during the different field campaigns (Fig. 5b). The diurnal variations at those remote sites (e.g., QOMS, LHG, NamCo, and Waliguan) located in the valley or at the top of the mountains were mostly controlled by the circulation of mountain-valley wind and the variation of PBL height during the whole day. A clear diurnal pattern with continuously decreasing concentrations during the daytime but relatively high concentrations at night was observed at QOMS. The minimum mass occurred at around ~15:00 in this valley site, mainly related to the strong down-slope glacier winds with high wind speed and enhanced PBL height in the afternoon (Zhang et al., 2018). Inversely, lower PM_1 mass from night to early morning whereas continuously increasing concentrations during the afternoon were observed at LHG and NamCo sites. The high mass concentrations in the afternoon at LHG were tightly associated with the

https://doi.org/10.5194/essd-2022-211
Preprint. Discussion started: 4 July 2022

transport of aerosols advected by the prevailing up-slope winds during that time. However, high concentration in the afternoon at NamCo might be influenced by the downward transmission of aerosols from the higher layer to ground surface and the enhanced aerosol plume transport from those relatively polluted western regions during afternoon (Xu et al., 2018). A relatively complex diurnal variation pattern of total PM_1 was observed at the top of Mt. Waliguan, which might be attributed to the common result of the variabilities in diffusion conditions (e.g., PBL height), wind directions (e.g., mountain-valley wind circulation), and air mass sources (e.g., enhanced air mass from northeast during the afternoon favored the transport of polluted aerosols from those industrial areas) (Zhang et al., 2019). The diurnal variation of PM_1 mass concentration was relatively stable at Motuo besides the two weak peaks in the late morning and evening that possibly related to the combustion emissions of biofuels from local domestic activities in that county. The PM_1 mass at Bayanbulak was relatively low and varied stably throughout the entire day due to its dominated background aerosols. Different with those remote sites, clear diurnal variation pattern with two obviously sharp peaks around 8:00–9:00 and 20:00–21:00 was found at the urban site in Lhasa, which could be attributed to those dominated primary aerosol sources from vehicle exhausts, cooking, and biomass burning emissions during the morning and evening rush hours (Zhao et al., 2022). Although the diurnal variations of total PM_1 were mainly affected by the variabilities in mountain-valley wind circulation and PBL height in those remote sites and primary emissions in the urban site in this study, the daytime photochemical oxidation and nighttime aqueous-phase reactions were also the two important formation pathways of secondary inorganic and organic aerosol species. This could be revealed clearly by those identified oxygenated OA (OOA) components at almost all the sites, which commonly showed continuously increasing concentration in the afternoon (Xu et al., 2018; Zhang et al., 2018; Zhang et al., 2019; Zhao et al., 2022).

4.5 High-resolution mass spectrum and elemental ratios of organic aerosol

The OA HRMS and elemental ratios were determined to recognize the possible sources, formation and evolution mechanisms, oxidation states of these complex OA components at each site. The average O/C ratios of OAs among the seven field campaigns were compared directly in boxplot in Fig. 6a. Obviously, the average O/C ratios of OAs were generally near to or larger than 1.0 at those remote sites of QOMS, Motuo, NamCo, Waliguan, and LHG, whereas a lower O/C ratio of ~0.69 was measured

https://doi.org/10.5194/essd-2022-211
Preprint. Discussion started: 4 July 2022

at Bayanbulak and a more lower O/C ratio of 0.44 was observed at the urban site in Lhasa. This difference in O/C ratios was mainly attributed to the different OA sources and aging processes among different sites. As mentioned above, atmospheric aerosols in those remote sites in the TP were generally related to the long-range transport aerosols from its surrounding areas, hence the OAs were overall well-mixed and highly aged during the transport from source region to the TP remote sites (Xu et al., 2018; Zhang et al., 2018; Zhang et al., 2019). However, local fresh OAs emitted from the residential activities (e.g., cooking, traffic exhausts, and biomass burning) dominated the total OA at urban Lhasa (Zhao et al., 2022), which finally resulted a relatively low O/C ratio. This difference could also be found in previous AMS studies in China, e.g., higher O/C ratios of 0.98, 1.11, and 1.16 were measured at these remote sites in Mt. Wuzhi (Zhu et al., 2016), Mt. Yulong (Zheng et al., 2017), and LHG (Xu et al., 2015), however, O/C ratios of OAs were almost lower than 0.5 at most urban sites (Zhou et al., 2020). The Van Krevelen diagram (H/C versus O/C), a widely used approach to depict the changes in the elemental composition of OA stemming from atmospheric aging processing, was displayed in Figure 6b. An overall slope of −0.66 was observed for the bulk OAs among the seven field measurement campaigns in our study, which was comparable to those of −0.58 and −0.47 for different synthesized datasets from diverse field observations in previous researches (Chen et al., 2015; Zhou et al., 2020).

The average OA HRMSs between the remote (Waliguan as example in this study) and urban (Lhasa) sites were further compared directly in Fig. 6c to investigate their inherent difference in ion-compositions. Obviously, the OA HRMSs were distinctly different between the two different types of sites. *m*/*z* 44 (composed totally by CO_2^+), one of the most reliable markers of OOA, was the base peak (18%) in the OA HRMS at Waliguan site. The CO_2^+ and its related four ions (CO^+, H_2O^+, HO^+ and O^+) together contributed more than 41% of the total OA signals. Furthermore, the two oxygenated ion fragments ($C_xH_yO_1^+$ and $C_xH_yO_2^+$) contributed as higher as 66% of the total OA signals, as shown in pie chart in Fig. 6c. All these features demonstrated the overall highly oxygenated OA nature in those remote background sites in the TP. Differently, the OA HRMS at Lhasa was remarkably similar to those observed at most urban cities. The four *m*/*z*s at 43, 55, 57, and 60, which have been regarded as important mass spectral tracers for less oxidized OA compounds and primary traffic, cooking, and biomass burning related emissions (Zhang et al., 2005a; Alfarra et al., 2007; He et al.,

https://doi.org/10.5194/essd-2022-211
Preprint. Discussion started: 4 July 2022

2010), showed significant contributions to the total OA signals in this urban site. Comparatively, the ion fragment of $C_xH_y^+$ contributed as higher as 64.5% of the total OA signals in Lhasa, whereas the two oxygenated ion fragments contributed only 33.6%. The high contribution of fresh ion fragments in the OA HRMS in Lhasa was comparable to those measured at other urban cities, such as 56% and 59% in Lanzhou (Xu et al., 2014b; Xu et al., 2016), 51.2% in Nanjing (Wang et al., 2016), and 51.2% in New York (Sun et al., 2011).

4.6 OA components from PMF source apportionment

Source apportionments of OA were performed using the PMF analysis on OA HRMS data during each aerosol field campaign in this study. Finally, 2−4 factor solutions were selected during the different field campaigns, as shown in Fig. 7. Due to the extremely limited local combustion activities but dominated aerosol sources from regional transport at those remote sites in the TP and its surroundings, only two secondary OOA factors with different oxidation degrees, i.e., a less oxidized OOA (LO-OOA) and a more oxidized OOA (MO-OOA), were identified during the NamCo, LHG, and Bayanbulak campaigns. On average, MO-OOA and LO-OOA, with average O/C ratios of 0.96 and 0.49, respectively, accounted for 59.0% and 41.0% of the total OA mass during the NamCo campaign. Comparably, the contributions of MO-OOA (average O/C of 1.12) and LO-OOA (average O/C of 0.55) to total OA mass were 66.3% and 33.7% during the Bayanbulak campaign. However, only 24.9% of MO-OOA and as higher as 75.1% of LO-OOA with relatively high O/C ratios of 1.29 and 1.08 were observed during the LHG campaign. Besides the two OOA factors, biomass-burning-related OA (BBOA) was another OA component that widely identified in the TP regions. The total OA mass was composed by 42.4% of MO-OOA, 43.9% of BBOA, and 13.9% of nitrogen-containing OA (NOA) at QOMS, with average O/C ratios of 1.34, 0.85, and 1.10, respectively. The high O/C ratio and more than half contributions from BBOA and NOA at QOMS was associated with the prevalent transport of biomass burning emissions from those polluted regions in South Asia to Himalaya and the inland TP regions during the pre-monsoon season (Cong et al., 2015; Zhang et al., 2018; Kang et al., 2019a). The total OA mass was composed by 34.4% of MO-OOA, 40.4% of relatively aged BBOA (agBBOA), 18.3% of BBOA, and 6.9% of traffic-related hydrocarbon-like OA (HOA) at Waliguan, with average O/C ratios of 1.42, 1.02, 0.69, and 0.33, respectively. The two BBOA components (particularly agBBOA) also showed

https://doi.org/10.5194/essd-2022-211
Preprint. Discussion started: 4 July 2022

enhanced contribution to total OA with the increasing OA mass concentration, e.g., significantly increased contribution from only ~10% to as high as 70% when OA mass varied from <1.0 μg m^{-3} to 7 μg m^{-3} (Zhang et al., 2019). In addition, source analysis has revealed that high contributions of the two BBOA components at Waliguan were associated with the regional transport of biomass burning emissions from the residential areas in northeastern Waliguan (Zhang et al., 2019). The total OA mass was composed by 36.9% of MO-OOA, 46.9% of LO-OOA, and 16.2% of BBOA at Motuo, with average O/C ratios of 1.30, 1.11, and 0.25, respectively. Comparatively, the BBOA factor at Motuo has relatively lower mass contribution and O/C ratio than those observed at QOMS and Waliguan, suggested that there was also weak local source from biofuels combustion around the county in spite of the dominant source was related to the regional transport. Four OA factors including an OOA component with O/C ratio of 0.54 and three primary OA components, i.e., a BBOA with O/C of 0.13, a cooking-related OA (COA) with O/C of 0.12, and a HOA with O/C of 0.11, were identified at the urban site in Lhasa, which were distinctly different with those observed at above remote sites. The three primary components contributed more than 60% of the total OA mass at Lhasa, suggesting the abundant primary aerosol sources from cooking, traffic vehicle exhausts, and biofuel combustion during the residential activities. In addition, the BBOA contribution increased obviously (up to 36%) during a grand local festival at Lhasa, suggesting the crucial aerosol source from biomass burning during religious activities in the city (Zhao et al., 2022). In summary, distinct types of OA components with different O/C ratios were identified at different sites, indicating the different oxidation states of OA in the different TP regions, especially between those remote sites and urban site, due to their distinct aerosol sources.

4.7 Number concentration and size distribution of submicron aerosols

Real-time online measurements of the size distribution of number concentration of submicron particles were also conducted simultaneously using the SMPS instruments during four field campaigns. Measurement of the particle number size distribution (PNSD) was not only an important auxiliary data to calibrate and verify the accuracy of HR-ToF-AMS data, but also very useful for studying the formation and growth mechanisms of aerosol particles in the atmosphere. The high-resolution temporal variations of the PNSDs during the QOMS, Motuo, LHG, and Lhasa campaigns were displayed in image-plots in Fig. 8a. Obviously, the PNSDs varied dynamically during

https://doi.org/10.5194/essd-2022-211
Preprint. Discussion started: 4 July 2022

the entire measurement period at each site and showed distinctly different number concentration level and size distribution pattern among the four different campaigns. On average, the total number concentrations were 709.3 and 3994.4 cm^{-3} for submicron particles between 14.6 and 661.2 nm in D_m at QOMS and Lhasa, while 1639.2 and 1462.0 cm^{-3} for submicron particles between 10.9 and 495.8 nm in D_m at Motuo and LHG. It was worth noting that the difference in particle number concentrations were not consistent with that in mass concentrations measured from the HR-ToF-AMSs among the four campaigns (Table 2). For example, the PM_1 mass concentration at Lhasa was comparable to that at QOMS (4.7 versus 4.4 μg m^{-3}), but the number concentration at Lhasa was more than five times the latter. This discrepancy may be related to the distinctly different sizes and oxidation states of particles at different sites. As discussed above, submicron aerosols at QOMS were overall highly aged due to the dominant long-range transported sources from the South Asia, whereas more fresh aerosols emitted from those residential activities like cooking, traffic vehicle exhausts, and biofuel combustion at Lhasa. The different sizes of submicron aerosols among the different TP regions could be clearly confirmed by both the peak diameters in the average size distributions of mass and number concentrations in Fig. 5a and 8b, respectively. For example, 510.2 and 430.5 nm in D_{va} for the average OA mass size distributions and 109.4 and 131.0 nm in D_m for the average number size distributions were observed at QOMS and Motuo, respectively, whereas only 228.1 nm in D_{va} and 28.9 nm in D_m at Lhasa, correspondingly. Besides the primary emission sources from various residential combustion activities, the new particle formation (NPF) was another important source of fresh aerosol particles with small sizes in the global atmosphere (Kulmala et al., 2017). The NPF event is generally characterized by a rapid burst in nucleation mode followed by the subsequent growth into larger particles, as indicated obviously by the typical banana-shaped temporal developments in the PNSD (Dal Maso et al., 2005). As shown in Fig. 8a, a large number of banana-shaped variation patterns were observed obviously in the PNSD at Lhasa, suggesting the frequent occurrence of NPF at this urban region. Totally, 10 NPF events have been observed among all the 27 available days during the Lhasa campaign (Zhao et al., 2022).

4.8 Aerosol optical properties and light absorptions from BC and BrC

The optical properties of aerosol particles are crucial input parameters for the accurate estimation of aerosol radiative forcing in climate models, however, there are large

https://doi.org/10.5194/essd-2022-211
Preprint. Discussion started: 4 July 2022

uncertainties until now due to the still limited dataset in this remote region. In our project, the B_{scat}, B_{abs}, and SSA of fine particles at 405 nm were observed during four of field campaigns, i.e., QOMS, Motuo, Waliguan, and Lhasa, to explore the difference in aerosol optical properties at different regions. On average, the B_{scat} and B_{abs} at 405 nm during the four campaigns were 121.9, 44.9, 36.3, and 2.1 Mm^{-1} and 10.8, 7.0, 4.1, and 1.9 Mm^{-1}, respectively, which finally resulted average SSA values of 0.89, 0.83, 0.86, and 0.52, correspondingly (Fig. 9a and Table 2). The highest B_{scat}, B_{abs}, and SSA values were all observed at QOMS although the PM_1 mass at this site was lower than those at the other three sites, which might be attributed to the different aerosol chemical compositions and the enhanced mass scattering and absorbing efficiencies. An obviously lower SSA at Lhasa compared with those at the other three remote sites suggested the overall fresh aerosols at the urban area. In contrast, aerosols at the three remote sites were highly aged, which resulted in significant photobleaching in BrC chromophores and obvious decrease in their light absorptivity at these sites.

In this study, real-time online measurements of particle B_{abs} at seven fixed wavelengths were also conducted using an aethalometer at QOMS, NamCo, and Waliguan, respectively, to explore the regional difference in aerosol absorption properties. Overall, the muti-wavelength B_{abs} decreased significantly with the increasing wavelength during all the three measurement campaigns, with different fitted AAE values to be 1.73, 1.28, and 1.12, respectively (Fig. 9b). The average B_{abs} at 370 nm was 13.40, 3.25, and 2.66 Mm^{-1} at the three sites, respectively (Table 2). Comparatively, the B_{abs} at 370 nm at QOMS was five times as high as that at Waliguan although its relatively low PM_1 mass was observed, mainly as a result of the higher contribution of light-absorbing aerosol components in the southern TP regions (e.g., OA and BC together contributed nearly 80% of the total PM_1 at QOMS whereas this contribution decreased to only 37.5% at Waliguan). The obviously higher AAE at QOMS also suggested the dominant light-absorbing contribution of BrC or important lensing effect of non-BC materials coated on BC cores at this site (Zhang et al., 2021). As shown in the inserted plots in Fig. 9b, although both $B_{abs,BC}$ and $B_{abs,BrC}$ decreased significantly with the increasing wavelength, their contributions to total B_{abs} ($fB_{abs,BC}$ and $fB_{abs,BrC}$) varied inversely. BC was the major light-absorbing component at all the three sites, which contributions to total B_{abs} at 370 nm were 66.9%, 78.7%, and 77.6% at QOMS, NamCo, and Waliguan sites and increased apparently with the increasing wavelengths (Table 2). BrC showed more

https://doi.org/10.5194/essd-2022-211
Preprint. Discussion started: 4 July 2022

important contributions to total B_{abs} at shorter wavelengths. For example, the averaged $B_{abs,BrC}$ at 370 nm were 4.42, 0.69, and 0.60 Mm^{-1} at the three sites, respectively, which finally contributed 33.1%, 21.3%, and 22.4% of the total B_{abs}, correspondingly. The significantly higher values of total B_{abs}, $B_{abs,BC}$, and $B_{abs,BrC}$ and the higher BrC contribution in the southern TP region might be related to the important contributions of light-absorbing carbonaceous aerosols from the transported biomass burning emissions (Xu et al., 2020, 2022).

4.9 Number concentration of cloud condensation nuclei

Cloud condensation nuclei (CCN), a unique class of atmospheric aerosol particles which could act as cloud droplets through the condensation of supersaturated water vapor on those preexisting particles, played important roles in the formation of clouds and atmospheric precipitation, and furthermore influenced the atmospheric physics and chemistry, the regional climate, as well as the hydrological cycle (Andreae and Rosenfeld, 2008). During the TP field campaigns, real-time online measurements of CCN number concentrations were deployed at the different TP regions (Waliguan and LHG). Normally, the temporal variation of CCN number concentration showed consistent variation trend with those of total number concentration from the SMPS measurement or total PM_1 mass concentration from the HR-ToF-AMS measurement during each campaign. On average, the CCN number concentrations were 507.0, 805.1, 1073.3, 1230.6, and 1336.6 cm^{-3}, respectively, at different *SS* values of 0.2%, 0.4%, 0.6%, 0.8%, and 1.0% at Waliguan, while those average values decreased obviously to 83.9, 344.3, 429.9, 480.8, and 516.1 cm^{-3} at LHG, correspondingly (Table 2). The lower CCN number concentrations at LHG compared with those at Waliguan were consistent with the relatively lower PM_1 mass loading (2.7 vs. 9.1 μg m^{-3}) at the former site. The CCN number concentrations at the two TP sites were almost an order of magnitude lower than those observed in the polluted urban atmospheres or direct emissions of unique combustion smokes, e.g., 12963 cm^{-3} (*SS* = 0.70%) in Wuqing and 9890 cm^{-3} (*SS* = 0.86%) in Beijing in the polluted North China Plain (Deng et al., 2011; Gunthe et al., 2011), 7913 cm^{-3} (*SS* = 0.70%) at Panyu in the Pearl River Delta, as well as 11565 cm^{-3} (*SS* = 0.87%) and 10000 cm^{-3} (*SS* = 0.80%) during unique biomass burning plumes (Rose et al., 2010; Zhang et al., 2020b). However, these values were comparable to those (228−2150 cm^{-3} with *SS* of 0.87%) measured at eight remote marine sites in the South China Sea and that of 941 cm^{-3} (*SS* = 0.74%) measured in the amazon rain

https://doi.org/10.5194/essd-2022-211
Preprint. Discussion started: 4 July 2022

forest. All these comparisons again suggested the overall clean atmospheric condition in the TP.

4.10 Concentrations of gaseous pollutants

High-resolution real-time online measurements of the gaseous precursor pollutants, including the CO_2, CO, O_3, SO_2, NO, NO_2, and NO_X, were performed during the two field campaigns at Lhasa and Motuo. All these gaseous pollutants generally showed different and interesting temporal variation trends and diurnal variation patterns during the entire measurement period, reflecting their distinctly different emission sources, sinks, and transformation mechanisms. Average concentrations of CO_2 during the two campaigns were 416.2 ppm for Lhasa and 382.0 ppm for Motuo, with high concentrations at night and continuously decreasing concentrations from early morning to afternoon during both the two campaigns. The decreasing concentration of CO_2 in the day might be mainly attributed to the daytime consumption of CO_2 by the intense plant photosynthesis in addition to the favorable dilution conditions related to the increasing PBL height. The average concentration of CO was 0.47 ppm at Motuo with relatively stable variations during the entire day due to the possibly limited primary emission sources at this remote site, while the measurement of CO at Lhasa was not performed due to the instrumental malfunction. The surface O_3 showed almost inverse diurnal variation pattern compared with that of CO_2 due to its dominant photochemical formation pathway during the daytime and finally had average concentrations of 36.7 and 33.5 ppb at Lhasa and Motuo, respectively. The SO_2 generally exhibited relatively flat diurnal variations compared with the others, with average values of 9.8 and 3.0 ppb, respectively, during the two campaigns. The average concentrations of NO, NO_2, and NO_X were 4.6, 8.7, and 13.3 ppb at Lhasa, which were more than seven times higher than those at Motuo. Meantime, diurnal variation of the three gaseous pollutants showed obvious bimodal pattern in the morning and evening at Lhasa, mainly attributed to the important urban traffic emissions during the corresponding rush hour periods.

5 Data availability

All the high-resolution online measurement datasets of aerosol physical, chemical, and optical properties over the Tibetan Plateau and its surroundings in our observation project have been released and are available to download from the National Cryosphere Desert Data Center (https://doi.org/10.12072/ncdc.NIEER.db2200.2022; Xu, 2022).

https://doi.org/10.5194/essd-2022-211
Preprint. Discussion started: 4 July 2022

The entire datasets are provided in an Excel file with eight worksheets. A brief description about the dataset including the dataset name, observation stations, sampling periods, online instruments, and corresponding references is introduced in the first sheet, while the rest seven sheets presented the high-resolution measurement data from those online instruments (HR-ToF-AMS, SMPS, PAX, aethalometer, CCN-100, and gas analyzers) during the seven observation campaigns, respectively.

6 Conclusions

The real-time online measurements of aerosol physicochemical and optical properties, especially the high-resolution size-resolved chemical characteristics and sources of submicron aerosols, were performed at different sites of the TP and its surroundings by our research team since 2015. The purpose of carrying out these difficult observational studies over the TP is aimed to understand the mass concentration level of atmospheric aerosols in this remote background region and recognize the regional differences on aerosol sources and physicochemical and optical properties among different TP regions, which finally provide remarkably valuable data in exactly simulating the radiative forcing and other potential impacts of atmospheric aerosols in this remote region in future climatic models.

In this paper, a comprehensive high-time-resolution (hourly scale) dataset of aerosol physical, chemical, and optical properties over the TP and its surroundings based on multi-years online in-situ observations was presented and discussed. Totally, seven aerosol field measurements were conducted at QOMS, Motuo, NamCo, Waliguan, LHG, Bayanbulak, and Lhasa in the different regions of TP and its surroundings by deploying multiple online instruments such as HR-ToF-AMS, SMPS, PAX, Aethalometer, CCN-100, and gas analyzers. The related datasets normally presented the temporal and diurnal variations and size distribution patterns of PM_1 chemical compositions, the standard high-resolution mass spectra and temporal variations of OA components, the temporal variations of particle number size distribution, particle light scattering and absorption coefficients, particle light absorptions from different carbonaceous substances of BC and BrC, CCN number concentrations at different supersaturation, and concentrations of gaseous pollutants in each campaign. The datasets are presented in the form of Excel file and available to download from the National Cryosphere Desert Data Center.

https://doi.org/10.5194/essd-2022-211
Preprint. Discussion started: 4 July 2022

The datasets well elucidated the regional differences in aerosol properties and sources at the different TP regions. In conclusion, atmospheric aerosols in the southern TP region generally related to the transported biomass burning emissions from polluted regions in South Asia, which finally resulted the high mass contributions (>70%) of carbonaceous aerosols (OA and BC), the overall neutralized PM_1 and even more excesses of ammonium, as well as the enhanced light absorption capability of the light-absorbing BC and BrC. Differently, secondary inorganic species (particularly the sulfate) contributed significantly to total PM_1 in the northern TP regions due to the regional transport of anthropogenic aerosol and gaseous precursor emissions from those industrial urban areas in northwestern China. In addition, different with those well-mixed, highly-aged, and regional transported aerosols in the remote sites, atmospheric aerosols in the urban Lhasa were mainly emitted from those primary sources like cooking, traffic vehicle exhausts, and biofuel combustion during the residential activities, and therefore, those aerosol particles were relatively fresh with small size and low oxidation degree but high frequency of NPF origins.

Appendix A: Main Abbreviations

TP	Tibetan Plateau
HR-ToF-AMS	high-resolution time-of-flight aerosol mass spectrometer
SMPS	scanning mobility particle sizer
PAX	photo-acoustic extinctiometer
CCN	cloud condensation nuclei
SS	supersaturation
PM_1	submicron aerosol
BC	black carbon
BrC	brown carbon
OA	organic aerosol
SNA	sulfate, nitrate, and ammonium
D_m	mobility diameter
D_{va}	aerodynamic diameter
IE	ionization efficiency
RIE	relative ionization efficiency
CE	collection efficiency
CDCE	composition-dependent collection efficiency
S/N	signal-to-noise ratio
m/*z*	mass-to-charge ratio
HRMS	high-resolution mass spectrum
RH	relative humidity
ANMF	ammonium nitrate mass fraction
PBL	planetary boundary layer
O/C	oxygen-to-carbon ratio
H/C	hydrogen-to-carbon ratio

https://doi.org/10.5194/essd-2022-211
Preprint. Discussion started: 4 July 2022

N/C	nitrogen-to-carbon ratio
OM/OC	organic matter-to-organic carbon ratio
PMF	positive matrix factorization
OOA	oxygenated organic aerosol
LO-OOA	less oxidized oxygenated organic aerosol
MO-OOA	more oxidized oxygenated organic aerosol
BBOA	biomass-burning-related organic aerosol
agBBOA	aged biomass-burning-related organic aerosol
NOA	nitrogen-containing organic aerosol
HOA	traffic-related hydrocarbon-like organic aerosol
COA	cooking-related organic aerosol
PNSD	particle number size distribution
NPF	new particle formation
B_{scat}	light scattering coefficient
B_{abs}	light absorption coefficient
B_{ext}	light extinction coefficient
SSA	single scattering albedo
AAE	absorption Ångström exponents
$B_{abs,BC}$	light absorption coefficient from BC
$B_{abs,BrC}$	light absorption coefficient from BrC

Author Contributions. JX designed the study, XZ, WZ, and JX wrote the manuscript. JX and SK organized and supervised the field measurement campaigns, JX, XZ, WZ, LZ, MZ, JS, JShi, YL, CX, YT, KL, XG, and QZ conducted the field measurements, JX, XZ, WZ, and YT analyzed the data. All authors reviewed and commented on the final form of the manuscript.

Competing interests. The authors declared that they have no competing interests.

Acknowledgements. We appreciate all of our colleagues and collaborators who participated the aerosol field measurements, maintained the instruments, analyzed the data, and commented on the manuscript. We also show great thanks to all the observation stations in this study for their logistical supports with the field campaigns.

Financial support. This work was supported by the National Natural Science Foundation of China (41977189 and 41771079), the Second Tibetan Plateau Scientific Expedition and Research program (STEP) (2019QZKK0605), the Strategic Priority Research Program of Chinese Academy of Sciences, Pan-Third Pole Environment Study for a Green Silk Road (Pan-TPE) (XDA20040501), the State Key Laboratory of Cryospheric Sciences Scientific Research Foundation (SKLCS-ZZ-2022), and the Chinese Academy of Sciences Hundred Talents Program.

https://doi.org/10.5194/essd-2022-211
Preprint. Discussion started: 4 July 2022

References

Aiken, A. C., DeCarlo, P. F., Kroll, J. H., Worsnop, D. R., Huffman, J. A., Docherty, K. S., Ulbrich, I. M., Mohr, C., Kimmel, J. R., Sueper, D., Sun, Y., Zhang, Q., Trimborn, A., Northway, M., Ziemann, P. J., Canagaratna, M. R., Onasch, T. B., Alfarra, M. R., Prevot, A. S. H., Dommen, J., Duplissy, J., Metzger, A., Baltensperger, U., and Jimenez, J. L.: O/C and OM/OC ratios of primary, secondary, and ambient organic aerosols with high-resolution time-of-flight aerosol mass spectrometry, Environ. Sci. Technol., 42, 4478-4485, 10.1021/es703009q, 2008.

Aiken, A. C., Salcedo, D., Cubison, M. J., Huffman, J. A., DeCarlo, P. F., Ulbrich, I. M., Docherty, K. S., Sueper, D., Kimmel, J. R., Worsnop, D. R., Trimborn, A., Northway, M., Stone, E. A., Schauer, J. J., Volkamer, R. M., Fortner, E., de Foy, B., Wang, J., Laskin, A., Shutthanandan, V., Zheng, J., Zhang, R., Gaffney, J., Marley, N. A., Paredes-Miranda, G., Arnott, W. P., Molina, L. T., Sosa, G., and Jimenez, J. L.: Mexico City aerosol analysis during MILAGRO using high resolution aerosol mass spectrometry at the urban supersite (T0) – Part 1: Fine particle composition and organic source apportionment, Atmos. Chem. Phys., 9, 6633-6653, 10.5194/acp-9-6633-2009, 2009.

Alfarra, M. R., Prevot, A. S. H., Szidat, S., Sandradewi, J., Weimer, S., Lanz, V. A., Schreiber, D., Mohr, M., and Baltensperger, U.: Identification of the mass spectral signature of organic aerosols from wood burning emissions, Environ. Sci. Technol., 41, 5770-5777, 10.1021/es062289b, 2007.

Allan, J. D., Delia, A. E., Coe, H., Bower, K. N., Alfarra, M. R., Jimenez, J. L., Middlebrook, A. M., Drewnick, F., Onasch, T. B., Canagaratna, M. R., Jayne, J. T., and Worsnop, D. R.: A generalised method for the extraction of chemically resolved mass spectra from Aerodyne aerosol mass spectrometer data, J. Aerosol Sci., 35, 909-922, 10.1016/j.jaerosci.2004.02.007, 2004.

An, Y., Xu, J., Feng, L., Zhang, X., Liu, Y., Kang, S., Jiang, B., and Liao, Y.: Molecular characterization of organic aerosol in the Himalayas: insight from ultra-high-resolution mass spectrometry, Atmos. Chem. Phys., 19, 1115-1128, 10.5194/acp-19-1115-2019, 2019.

Andreae, M. O., and Rosenfeld, D.: Aerosol–cloud–precipitation interactions. Part 1. The nature and sources of cloud-active aerosols, Earth-Science Reviews, 89, 13-41, 10.1016/j.earscirev.2008.03.001, 2008.

Bonasoni, P., Laj, P., Marinoni, A., Sprenger, M., Angelini, F., Arduini, J., Bonafè, U., Calzolari, F., Colombo, T., Decesari, S., Di Biagio, C., di Sarra, A. G., Evangelisti, F., Duchi, R., Facchini, M. C., Fuzzi, S., Gobbi, G. P., Maione, M., Panday, A., Roccato, F., Sellegri, K., Venzac, H., Verza, G. P., Villani, P., Vuillermoz, E., and Cristofanelli, P.: Atmospheric Brown Clouds in the Himalayas: first two years of continuous observations at the Nepal Climate Observatory-Pyramid (5079 m), Atmos. Chem. Phys., 10, 7515-7531, 10.5194/acp-10-7515-2010, 2010.

Bond, T. C., Streets, D. G., Yarber, K. F., Nelson, S. M., Woo, J.-H., and Klimont, Z.: A technology-based global inventory of black and organic carbon emissions from combustion, J. Geophys. Res., 109, D14203, 10.1029/2003jd003697, 2004.

Canagaratna, M. R., Jimenez, J. L., Kroll, J. H., Chen, Q., Kessler, S. H., Massoli, P., Hildebrandt Ruiz, L., Fortner, E., Williams, L. R., Wilson, K. R., Surratt, J. D., Donahue, N. M., Jayne, J. T., and Worsnop, D. R.: Elemental ratio measurements of organic compounds using aerosol mass spectrometry: characterization, improved calibration, and implications, Atmos. Chem. Phys., 15, 253-272, 10.5194/acp-15-253-2015, 2015.

Cao, J., Xu, B., He, J., Liu, X., Han, Y., Wang, G., and Zhu, C.: Concentrations, seasonal variations, and transport of carbonaceous aerosols at a remote Mountainous region in western China, Atmos. Environ., 43, 4444-4452, 10.1016/j.atmosenv.2009.06.023, 2009.

Chen, F., Ding, L., Piao, S., Zhou, T., Xu, B., Yao, T., and Li, X.: The Tibetan Plateau as the engine for Asian environmental change: the Tibetan Plateau Earth system research into a new era, Science Bulletin, 66, 1263-1266, 10.1016/j.scib.2021.04.017, 2021.

Chen, P., Kang, S., Li, C., Zhang, Q., Guo, J., Tripathee, L., Zhang, Y., Li, G., Gul, C., Cong, Z., Wan, X., Niu, H., Panday, A. K., Rupakheti, M., and Ji, Z.: Carbonaceous aerosol characteristics on the Third Pole: A primary study based on the Atmospheric Pollution and Cryospheric Change (APCC) network, Environ. Pollut., 253, 49-60, 10.1016/j.envpol.2019.06.112, 2019.

Chen, Q., Heald, C. L., Jimenez, J. L., Canagaratna, M. R., Zhang, Q., He, L. Y., Huang, X. F., Campuzano-Jost, P., Palm, B. B., Poulain, L., Kuwata, M., Martin, S. T., Abbatt, J. P. D., Lee, A. K. Y., and Liggio, J.: Elemental composition of organic aerosol: The gap between ambient and laboratory measurements, Geophys. Res. Lett., 42, 4182-4189, 10.1002/2015gl063693, 2015.

Cong, Z., Kang, S., Kawamura, K., Liu, B., Wan, X., Wang, Z., Gao, S., and Fu, P.: Carbonaceous aerosols on the south edge of the Tibetan Plateau: concentrations, seasonality and sources, Atmos. Chem. Phys., 15, 1573-1584, 10.5194/acp-15-1573-2015, 2015.

Cui, Y. Y., Liu, S., Bai, Z., Bian, J., Li, D., Fan, K., McKeen, S. A., Watts, L. A., Ciciora, S. J., and Gao,

https://doi.org/10.5194/essd-2022-211
Preprint. Discussion started: 4 July 2022

R.-S.: Religious burning as a potential major source of atmospheric fine aerosols in summertime Lhasa on the Tibetan Plateau, Atmos. Environ., 181, 186-191, 10.1016/j.atmosenv.2018.03.025, 2018.

Dal Maso, M., Kulmala, M., Riipinen, I., Wagner, R., Hussein, T., Aalto, P. P., and Lehtinen, K. E. J.: Formation and growth of fresh atmospheric aerosols: eight years of aerosol size distribution data from SMEAR II, Hyytiala, Finland, Boreal Environ. Res., 10, 323-336, 2005.

DeCarlo, P. F., Kimmel, J. R., Trimborn, A., Northway, M. J., Jayne, J. T., Aiken, A. C., Gonin, M., Fuhrer, K., Horvath, T., Docherty, K. S., Worsnop, D. R., and Jimenez, J. L.: Field-Deployable, High-Resolution, Time-of-Flight Aerosol Mass Spectrometer, Anal. Chem., 78, 8281-8289, 10.1021/ac061249n, 2006.

Deng, Z. Z., Zhao, C. S., Ma, N., Liu, P. F., Ran, L., Xu, W. Y., Chen, J., Liang, Z., Liang, S., Huang, M. Y., Ma, X. C., Zhang, Q., Quan, J. N., Yan, P., Henning, S., Mildenberger, K., Sommerhage, E., Schäfer, M., Stratmann, F., and Wiedensohler, A.: Size-resolved and bulk activation properties of aerosols in the North China Plain, Atmos. Chem. Phys., 11, 3835-3846, 10.5194/acp-11-3835-2011, 2011.

Dong, Z., Kang, S., Qin, D., Qin, X., Yan, F., Du, W., and Wei, T.: Temporal and diurnal analysis of trace elements in the Cryospheric water at remote Laohugou basin in northeast Tibetan Plateau, Chemosphere, 171, 386-398, 10.1016/j.chemosphere.2016.12.088, 2017.

Du, W., Sun, Y. L., Xu, Y. S., Jiang, Q., Wang, Q. Q., Yang, W., Wang, F., Bai, Z. P., Zhao, X. D., and Yang, Y. C.: Chemical characterization of submicron aerosol and particle growth events at a national background site (3295 m a.s.l.) on the Tibetan Plateau, Atmos. Chem. Phys., 15, 10811-10824, 10.5194/acp-15-10811-2015, 2015.

Duan, A. M., and Wu, G. X.: Role of the Tibetan Plateau thermal forcing in the summer climate patterns over subtropical Asia, Clim. Dyn., 24, 793-807, 10.1007/s00382-004-0488-8, 2005.

Freney, E. J., Sellegri, K., Canonaco, F., Boulon, J., Hervo, M., Weigel, R., Pichon, J. M., Colomb, A., Prévôt, A. S. H., and Laj, P.: Seasonal variations in aerosol particle composition at the puy-de-Dôme research station in France, Atmos. Chem. Phys., 11, 13047-13059, 10.5194/acp-11-13047-2011, 2011.

Fröhlich, R., Cubison, M. J., Slowik, J. G., Bukowiecki, N., Canonaco, F., Croteau, P. L., Gysel, M., Henne, S., Herrmann, E., Jayne, J. T., Steinbacher, M., Worsnop, D. R., Baltensperger, U., and Prévôt, A. S. H.: Fourteen months of on-line measurements of the non-refractory submicron aerosol at the Jungfraujoch (3580 m a.s.l.) – chemical composition, origins and organic aerosol sources, Atmos. Chem. Phys., 15, 11373-11398, 10.5194/acp-15-11373-2015, 2015.

Gunthe, S. S., Rose, D., Su, H., Garland, R. M., Achtert, P., Nowak, A., Wiedensohler, A., Kuwata, M., Takegawa, N., Kondo, Y., Hu, M., Shao, M., Zhu, T., Andreae, M. O., and Pöschl, U.: Cloud condensation nuclei (CCN) from fresh and aged air pollution in the megacity region of Beijing, Atmos. Chem. Phys., 11, 11023-11039, 10.5194/acp-11-11023-2011, 2011.

He, C., Li, Q. B., Liou, K. N., Zhang, J., Qi, L., Mao, Y., Gao, M., Lu, Z., Streets, D. G., Zhang, Q., Sarin, M. M., and Ram, K.: A global 3-D CTM evaluation of black carbon in the Tibetan Plateau, Atmos. Chem. Phys., 14, 7091-7112, 10.5194/acp-14-7091-2014, 2014.

He, L. Y., Lin, Y., Huang, X. F., Guo, S., Xue, L., Su, Q., Hu, M., Luan, S. J., and Zhang, Y. H.: Characterization of high-resolution aerosol mass spectra of primary organic aerosol emissions from Chinese cooking and biomass burning, Atmos. Chem. Phys., 10, 11535-11543, 10.5194/acp-10-11535-2010, 2010.

Jayne, J. T., Leard, D. C., Zhang, X. F., Davidovits, P., Smith, K. A., Kolb, C. E., and Worsnop, D. R.: Development of an aerosol mass spectrometer for size and composition analysis of submicron particles, Aerosol Sci. Technol., 33, 49-70, 10.1080/027868200410840, 2000.

Ji, Z., Kang, S., Cong, Z., Zhang, Q., and Yao, T.: Simulation of carbonaceous aerosols over the Third Pole and adjacent regions: distribution, transportation, deposition, and climatic effects, Clim. Dyn., 45, 2831-2846, 10.1007/s00382-015-2509-1, 2015.

Jimenez, J. L., Jayne, J. T., Shi, Q., Kolb, C. E., Worsnop, D. R., Yourshaw, I., Seinfeld, J. H., Flagan, R. C., Zhang, X., Smith, K. A., Morris, J. W., and Davidovits, P.: Ambient aerosol sampling using the Aerodyne Aerosol Mass Spectrometer, J. Geophys. Res., 108, 8425, 10.1029/2001jd001213, 2003.

Jimenez, J. L., Canagaratna, M. R., Donahue, N. M., Prevot, A. S., Zhang, Q., Kroll, J. H., DeCarlo, P. F., Allan, J. D., Coe, H., Ng, N. L., Aiken, A. C., Docherty, K. S., Ulbrich, I. M., Grieshop, A. P., Robinson, A. L., Duplissy, J., Smith, J. D., Wilson, K. R., Lanz, V. A., Hueglin, C., Sun, Y. L., Tian, J., Laaksonen, A., Raatikainen, T., Rautiainen, J., Vaattovaara, P., Ehn, M., Kulmala, M., Tomlinson, J. M., Collins, D. R., Cubison, M. J., Dunlea, E. J., Huffman, J. A., Onasch, T. B., Alfarra, M. R., Williams, P. I., Bower, K., Kondo, Y., Schneider, J., Drewnick, F., Borrmann, S., Weimer, S., Demerjian, K., Salcedo, D., Cottrell, L., Griffin, R., Takami, A., Miyoshi, T., Hatakeyama, S., Shimono, A., Sun, J. Y., Zhang, Y. M., Dzepina, K., Kimmel, J. R., Sueper, D., Jayne, J. T., Herndon, S. C., Trimborn, A. M., Williams, L. R., Wood, E. C., Middlebrook, A. M., Kolb, C. E., Baltensperger, U., and Worsnop, D. R.: Evolution of organic aerosols in the atmosphere, Science, 326, 1525-1529,

https://doi.org/10.5194/essd-2022-211
Preprint. Discussion started: 4 July 2022

10.1126/science.1180353, 2009.
Kang, S., Xu, Y., You, Q., Flügel, W.-A., Pepin, N., and Yao, T.: Review of climate and cryospheric change in the Tibetan Plateau, Environ. Res. Lett., 5, 015101, 10.1088/1748-9326/5/1/015101, 2010.
Kang, S., Chen, P., Li, C., Liu, B., and Cong, Z.: Atmospheric Aerosol Elements over the Inland Tibetan Plateau: Concentration, Seasonality, and Transport, Aerosol Air Qual. Res., 16, 789-800, 10.4209/aaqr.2015.05.0307, 2016.
Kang, S., Cong, Z., Wang, X., Zhang, Q., Ji, Z., Zhang, Y., and Xu, B.: The transboundary transport of air pollutants and their environmental impacts on Tibetan Plateau, Chin. Sci. Bull., 64, 2876-2884, 10.1360/tb-2019-0135, 2019a.
Kang, S., Zhang, Q., Qian, Y., Ji, Z., Li, C., Cong, Z., Zhang, Y., Guo, J., Du, W., Huang, J., You, Q., Panday, A. K., Rupakheti, M., Chen, D., Gustafsson, Ö., Thiemens, M. H., and Qin, D.: Linking atmospheric pollution to cryospheric change in the Third Pole region: current progress and future prospects, Natl. Sci. Rev., 6, 796-809, 10.1093/nsr/nwz031, 2019b.
Kang, S., Zhang, Y., Chen, P., Guo, J., Zhang, Q., Cong, Z., Kaspari, S., Tripathee, L., Gao, T., Niu, H., Zhong, X., Chen, X., Hu, Z., Li, X., Li, Y., Neupane, B., Yan, F., Rupakheti, D., Gul, C., Zhang, W., Wu, G., Yang, L., Wang, Z., and Li, C.: Black carbon and organic carbon dataset over the Third Pole, Earth System Science Data, 14, 683-707, 10.5194/essd-14-683-2022, 2022.
Kopacz, M., Mauzerall, D. L., Wang, J., Leibensperger, E. M., Henze, D. K., and Singh, K.: Origin and radiative forcing of black carbon transported to the Himalayas and Tibetan Plateau, Atmos. Chem. Phys., 11, 2837-2852, 10.5194/acp-11-2837-2011, 2011.
Kulmala, M., Kerminen, V. M., Petäjä, T., Ding, A. J., and Wang, L.: Atmospheric gas-to-particle conversion: why NPF events are observed in megacities?, Faraday Discussions, 200, 2017.
Laskin, A., Laskin, J., and Nizkorodov, S. A.: Chemistry of atmospheric brown carbon, Chem. Rev., 115, 4335-4382, 10.1021/cr5006167, 2015.
Lau, K. M., Kim, M. K., and Kim, K. M.: Asian summer monsoon anomalies induced by aerosol direct forcing: the role of the Tibetan Plateau, Clim. Dyn., 26, 855-864, 10.1007/s00382-006-0114-z, 2006.
Li, C., Bosch, C., Kang, S., Andersson, A., Chen, P., Zhang, Q., Cong, Z., Chen, B., Qin, D., and Gustafsson, O.: Sources of black carbon to the Himalayan-Tibetan Plateau glaciers, Nat. Commun., 7, 12574, 10.1038/ncomms12574, 2016a.
Li, C., Yan, F., Kang, S., Chen, P., Hu, Z., Gao, S., Qu, B., and Sillanpää, M.: Light absorption characteristics of carbonaceous aerosols in two remote stations of the southern fringe of the Tibetan Plateau, China, Atmos. Environ., 143, 79-85, 10.1016/j.atmosenv.2016.08.042, 2016b.
Li, Y. J., Sun, Y., Zhang, Q., Li, X., Li, M., Zhou, Z., and Chan, C. K.: Real-time chemical characterization of atmospheric particulate matter in China: A review, Atmos. Environ., 158, 270-304, 10.1016/j.atmosenv.2017.02.027, 2017.
Liu, Y., Sato, Y., Jia, R., Xie, Y., Huang, J., and Nakajima, T.: Modeling study on the transport of summer dust and anthropogenic aerosols over the Tibetan Plateau, Atmos. Chem. Phys., 15, 12581-12594, 10.5194/acp-15-12581-2015, 2015.
Liu, Y., Hua, S., Jia, R., and Huang, J.: Effect of Aerosols on the Ice Cloud Properties Over the Tibetan Plateau, J. Geophys. Res. Atmos., 124, 9594-9608, 10.1029/2019jd030463, 2019.
Ma, J., Brühl, C., He, Q., Steil, B., Karydis, V. A., Klingmüller, K., Tost, H., Chen, B., Jin, Y., Liu, N., Xu, X., Yan, P., Zhou, X., Abdelrahman, K., Pozzer, A., and Lelieveld, J.: Modeling the aerosol chemical composition of the tropopause over the Tibetan Plateau during the Asian summer monsoon, Atmos. Chem. Phys., 19, 11587-11612, 10.5194/acp-19-11587-2019, 2019.
Middlebrook, A. M., Bahreini, R., Jimenez, J. L., and Canagaratna, M. R.: Evaluation of Composition-Dependent Collection Efficiencies for the Aerodyne Aerosol Mass Spectrometer using Field Data, Aerosol Sci. Technol., 46, 258-271, 10.1080/02786826.2011.620041, 2012.
Paatero, P., and Tapper, U.: Positive matrix factorization: A non-negative factor model with optimal utilization of error estimates of data values, Environmetrics, 5, 111-126, 10.1002/env.3170050203, 1994.
Qiu, J.: The third pole, Nature, 454, 393-396, 10.1038/454393a, 2008.
Ramanathan, V., Ramana, M. V., Roberts, G., Kim, D., Corrigan, C., Chung, C., and Winker, D.: Warming trends in Asia amplified by brown cloud solar absorption, Nature, 448, 575-578, 10.1038/nature06019, 2007.
Rinaldi, M., Gilardoni, S., Paglione, M., Sandrini, S., Fuzzi, S., Massoli, P., Bonasoni, P., Cristofanelli, P., Marinoni, A., Poluzzi, V., and Decesari, S.: Organic aerosol evolution and transport observed at Mt. Cimone (2165 m a.s.l.), Italy, during the PEGASOS campaign, Atmos. Chem. Phys., 15, 11327-11340, 10.5194/acp-15-11327-2015, 2015.
Rose, D., Nowak, A., Achtert, P., Wiedensohler, A., Hu, M., Shao, M., Zhang, Y., Andreae, M. O., and Poschl, U.: Cloud condensation nuclei in polluted air and biomass burning smoke near the mega-city

https://doi.org/10.5194/essd-2022-211
Preprint. Discussion started: 4 July 2022

Guangzhou, China - Part 1: Size-resolved measurements and implications for the modeling of aerosol particle hygroscopicity and CCN activity, Atmos. Chem. Phys., 10, 3365-3383, 10.5194/acp-10-3365-2010, 2010.

Schmale, J., Schneider, J., Nemitz, E., Tang, Y. S., Dragosits, U., Blackall, T. D., Trathan, P. N., Phillips, G. J., Sutton, M., and Braban, C. F.: Sub-Antarctic marine aerosol: dominant contributions from biogenic sources, Atmos. Chem. Phys., 13, 8669-8694, 10.5194/acp-13-8669-2013, 2013.

Schueneman, M. K., Nault, B. A., Campuzano-Jost, P., Jo, D. S., Day, D. A., Schroder, J. C., Palm, B. B., Hodzic, A., Dibb, J. E., and Jimenez, J. L.: Aerosol pH indicator and organosulfate detectability from aerosol mass spectrometry measurements, Atmos. Meas. Tech., 14, 2237-2260, 10.5194/amt-14-2237-2021, 2021.

Sun, Y. L., Zhang, Q., Macdonald, A. M., Hayden, K., Li, S. M., Liggio, J., Liu, P. S. K., Anlauf, K. G., Leaitch, W. R., Steffen, A., Cubison, M., Worsnop, D. R., van Donkelaar, A., and Martin, R. V.: Size-resolved aerosol chemistry on Whistler Mountain, Canada with a high-resolution aerosol mass spectrometer during INTEX-B, Atmos. Chem. Phys., 9, 3095-3111, 10.5194/acp-9-3095-2009, 2009.

Sun, Y. L., Zhang, Q., Schwab, J. J., Demerjian, K. L., Chen, W. N., Bae, M. S., Hung, H. M., Hogrefe, O., Frank, B., Rattigan, O. V., and Lin, Y. C.: Characterization of the sources and processes of organic and inorganic aerosols in New York city with a high-resolution time-of-flight aerosol mass apectrometer, Atmos. Chem. Phys., 11, 1581-1602, 10.5194/acp-11-1581-2011, 2011.

Takami, A., Miyoshi, T., Shimono, A., and Hatakeyama, S.: Chemical composition of fine aerosol measured by AMS at Fukue Island, Japan during APEX period, Atmos. Environ., 39, 4913-4924, 10.1016/j.atmosenv.2005.04.038, 2005.

Ulbrich, I. M., Canagaratna, M. R., Zhang, Q., Worsnop, D. R., and Jimenez, J. L.: Interpretation of organic components from Positive Matrix Factorization of aerosol mass spectrometric data, Atmos. Chem. Phys., 9, 2891-2918, 10.5194/acp-9-2891-2009, 2009.

Van Damme, M., Erisman, J. W., Clarisse, L., Dammers, E., Whitburn, S., Clerbaux, C., Dolman, A. J., and Coheur, P.-F.: Worldwide spatiotemporal atmospheric ammonia (NH_3) columns variability revealed by satellite, Geophys. Res. Lett., 42, 8660-8668, 10.1002/2015gl065496, 2015.

Wan, X., Kang, S., Wang, Y., Xin, J., Liu, B., Guo, Y., Wen, T., Zhang, G., and Cong, Z.: Size distribution of carbonaceous aerosols at a high-altitude site on the central Tibetan Plateau (Nam Co Station, 4730ma.s.l.), Atmos. Res., 153, 155-164, 10.1016/j.atmosres.2014.08.008, 2015.

Wang, J., Ge, X., Chen, Y., Shen, Y., Zhang, Q., Sun, Y., Xu, J., Ge, S., Yu, H., and Chen, M.: Highly time-resolved urban aerosol characteristics during springtime in Yangtze River Delta, China: insights from soot particle aerosol mass spectrometry, Atmos. Chem. Phys., 16, 9109-9127, 10.5194/acp-16-9109-2016, 2016.

Wang, J., Zhang, Q., Chen, M., Collier, S., Zhou, S., Ge, X., Xu, J., Shi, J., Xie, C., Hu, J., Ge, S., Sun, Y., and Coe, H.: First Chemical Characterization of Refractory Black Carbon Aerosols and Associated Coatings over the Tibetan Plateau (4730 m a.s.l), Environ. Sci. Technol., 51, 14072-14082, 10.1021/acs.est.7b03973, 2017.

Xu, B., Cao, J., Hansen, J., Yao, T., Joswia, D. R., Wang, N., Wu, G., Wang, M., Zhao, H., Yang, W., Liu, X., and He, J.: Black soot and the survival of Tibetan glaciers, Proc. Natl. Acad. Sci. USA, 106, 22114-22118, 10.1073/pnas.0910444106, 2009.

Xu, J., Wang, Z., Yu, G., Qin, X., Ren, J., and Qin, D.: Characteristics of water soluble ionic species in fine particles from a high altitude site on the northern boundary of Tibetan Plateau: Mixture of mineral dust and anthropogenic aerosol, Atmos. Res., 143, 43-56, 10.1016/j.atmosres.2014.01.018, 2014a.

Xu, J., Zhang, Q., Chen, M., Ge, X., Ren, J., and Qin, D.: Chemical composition, sources, and processes of urban aerosols during summertime in northwest China: insights from high-resolution aerosol mass spectrometry, Atmos. Chem. Phys., 14, 12593-12611, 10.5194/acp-14-12593-2014, 2014b.

Xu, J., Zhang, Q., Wang, Z. B., Yu, G. M., Ge, X. L., and Qin, X.: Chemical composition and size distribution of summertime $PM_{2.5}$ at a high altitude remote location in the northeast of the Qinghai-Xizang (Tibet) Plateau: insights into aerosol sources and processing in free troposphere, Atmos. Chem. Phys., 15, 5069-5081, 10.5194/acp-15-5069-2015, 2015.

Xu, J., Shi, J., Zhang, Q., Ge, X., Canonaco, F., Prévôt, A. S. H., Vonwiller, M., Szidat, S., Ge, J., Ma, J., An, Y., Kang, S., and Qin, D.: Wintertime organic and inorganic aerosols in Lanzhou, China: sources, processes, and comparison with the results during summer, Atmos. Chem. Phys., 16, 14937-14957, 10.5194/acp-16-14937-2016, 2016.

Xu, J., Zhang, Q., Shi, J., Ge, X., Xie, C., Wang, J., Kang, S., Zhang, R., and Wang, Y.: Chemical characteristics of submicron particles at the central Tibetan Plateau: insights from aerosol mass spectrometry, Atmos. Chem. Phys., 18, 427-443, 10.5194/acp-18-427-2018, 2018.

Xu, J., Hettiyadura, A. P. S., Liu, Y., Zhang, X., Kang, S., and Laskin, A.: Regional Differences of Chemical Composition and Optical Properties of Aerosols in the Tibetan Plateau, J. Geophys. Res.

https://doi.org/10.5194/essd-2022-211
Preprint. Discussion started: 4 July 2022

Atmos., 125, 10.1029/2019jd031226, 2020.

Xu, J.: High-time-resolution dataset of atmospheric aerosols over the Tibetan Plateau and its surroundings (2015-2021), National Cryosphere Desert Data Center [Data set], 10.12072/ncdc.NIEER.db2200.2022, 2022.

Xu, J., Hettiyadura, A. P. S., Liu, Y., Zhang, X., Kang, S., and Laskin, A.: Atmospheric Brown Carbon on the Tibetan Plateau: Regional Differences in Chemical Composition and Light Absorption Properties, Environmental Science & Technology Letters, 9, 219-225, 10.1021/acs.estlett.2c00016, 2022.

Yang, J., Ji, Z., Kang, S., and Tripathee, L.: Contribution of South Asian biomass burning to black carbon over the Tibetan Plateau and its climatic impact, Environ. Pollut., 270, 116195, 10.1016/j.envpol.2020.116195, 2021.

Yao, T., Thompson, L., Mosbrugger, V., Zhang, F., Ma, Y., Luo, T., Xu, B., Yang, X., Joswiak, D. R., Wang, W., Joswiak, M. E., Devkota, L. P., Tayal, S., Jilani, R., and Fayziev, R.: Third Pole Environment (TPE), Environ. Dev., 3, 52-64, 10.1016/j.envdev.2012.04.002, 2012.

Yao, T., Xue, Y., Chen, D., Chen, F., Thompson, L., Cui, P., Koike, T., Lau, W. K. M., Lettenmaier, D., Mosbrugger, V., Zhang, R., Xu, B., Dozier, J., Gillespie, T., Gu, Y., Kang, S., Piao, S., Sugimoto, S., Ueno, K., Wang, L., Wang, W., Zhang, F., Sheng, Y., Guo, W., Ailikun, Yang, X., Ma, Y., Shen, S. S. P., Su, Z., Chen, F., Liang, S., Liu, Y., Singh, V. P., Yang, K., Yang, D., Zhao, X., Qian, Y., Zhang, Y., and Li, Q.: Recent Third Pole's Rapid Warming Accompanies Cryospheric Melt and Water Cycle Intensification and Interactions between Monsoon and Environment: Multidisciplinary Approach with Observations, Modeling, and Analysis, Bull. Am. Meteorol. Soc., 100, 423-444, 10.1175/bams-d-17-0057.1, 2019.

You, Q., Cai, Z., Pepin, N., Chen, D., Ahrens, B., Jiang, Z., Wu, F., Kang, S., Zhang, R., Wu, T., Wang, P., Li, M., Zuo, Z., Gao, Y., Zhai, P., and Zhang, Y.: Warming amplification over the Arctic Pole and Third Pole: Trends, mechanisms and consequences, Earth-Science Reviews, 217, 103625, 10.1016/j.earscirev.2021.103625, 2021.

Zhang, M., Zhao, C., Cong, Z., Du, Q., Xu, M., Chen, Y., Chen, M., Li, R., Fu, Y., Zhong, L., Kang, S., Zhao, D., and Yang, Y.: Impact of topography on black carbon transport to the southern Tibetan Plateau during the pre-monsoon season and its climatic implication, Atmos. Chem. Phys., 20, 5923-5943, 10.5194/acp-20-5923-2020, 2020a.

Zhang, N., Cao, J., Liu, S., Zhao, Z., Xu, H., and Xiao, S.: Chemical composition and sources of $PM_{2.5}$ and TSP collected at Qinghai Lake during summertime, Atmos. Res., 138, 213-222, 10.1016/j.atmosres.2013.11.016, 2014.

Zhang, Q., Alfarra, M. R., Worsnop, D. R., Allan, J. D., Coe, H., Canagaratna, M. R., and Jimenez, J. L.: Deconvolution and quantification of hydrocarbon-like and oxygenated organic aerosols based on aerosol mass spectrometry, Environ. Sci. Technol., 39, 4938-4952, 10.1021/es048568l, 2005a.

Zhang, Q., Canagaratna, M. R., Jayne, J. T., Worsnop, D. R., and Jimenez, J. L.: Time- and size-resolved chemical composition of submicron particles in Pittsburgh: Implications for aerosol sources and processes, J. Geophys. Res. Atmos., 110, D07S09, 10.1029/2004jd004649, 2005b.

Zhang, Q., Jimenez, J. L., Canagaratna, M. R., Allan, J. D., Coe, H., Ulbrich, I., Alfarra, M. R., Takami, A., Middlebrook, A. M., Sun, Y. L., Dzepina, K., Dunlea, E., Docherty, K., DeCarlo, P. F., Salcedo, D., Onasch, T., Jayne, J. T., Miyoshi, T., Shimono, A., Hatakeyama, S., Takegawa, N., Kondo, Y., Schneider, J., Drewnick, F., Borrmann, S., Weimer, S., Demerjian, K., Williams, P., Bower, K., Bahreini, R., Cottrell, L., Griffin, R. J., Rautiainen, J., Sun, J. Y., Zhang, Y. M., and Worsnop, D. R.: Ubiquity and dominance of oxygenated species in organic aerosols in anthropogenically-influenced Northern Hemisphere midlatitudes, Geophys. Res. Lett., 34, L13801, 10.1029/2007gl029979, 2007a.

Zhang, Q., Jimenez, J. L., Worsnop, D., and Canagaratna, M.: A case study of urban particle acidity and its influence on secondary organic aerosol, Environ. Sci. Technol., 41, 3213-3219, 10.1021/es061812j, 2007b.

Zhang, Q., Jimenez, J. L., Canagaratna, M. R., Ulbrich, I. M., Ng, N. L., Worsnop, D. R., and Sun, Y.: Understanding atmospheric organic aerosols via factor analysis of aerosol mass spectrometry: a review, Anal. Bioanal. Chem., 401, 3045-3067, 10.1007/s00216-011-5355-y, 2011.

Zhang, R., Wang, Y., He, Q., Chen, L., Zhang, Y., Qu, H., Smeltzer, C., Li, J., Alvarado, L. M. A., Vrekoussis, M., Richter, A., Wittrock, F., and Burrows, J. P.: Enhanced trans-Himalaya pollution transport to the Tibetan Plateau by cut-off low systems, Atmos. Chem. Phys., 17, 3083-3095, 10.5194/acp-17-3083-2017, 2017.

Zhang, X., Xu, J., Kang, S., Liu, Y., and Zhang, Q.: Chemical characterization of long-range transport biomass burning emissions to the Himalayas: insights from high-resolution aerosol mass spectrometry, Atmos. Chem. Phys., 18, 4617–4638, 10.5194/acp-18-4617-2018, 2018.

Zhang, X., Xu, J., Kang, S., Zhang, Q., and Sun, J.: Chemical characterization and sources of submicron

https://doi.org/10.5194/essd-2022-211
Preprint. Discussion started: 4 July 2022

aerosols in the northeastern Qinghai–Tibet Plateau: insights from high-resolution mass spectrometry, Atmos. Chem. Phys., 19, 7897-7911, 10.5194/acp-19-7897-2019, 2019.

Zhang, X., Xu, J., and Kang, S.: Chemical characterization of submicron particulate matter (PM_1) emitted by burning highland barley in the northeastern part of the Qinghai–Tibet Plateau, Atmos. Environ., 224, 117351, 10.1016/j.atmosenv.2020.117351, 2020b.

Zhang, X., Xu, J., Kang, S., Sun, J., Shi, J., Gong, C., Sun, X., Du, H., Ge, X., and Zhang, Q.: Regional Differences in the Light Absorption Properties of Fine Particulate Matter Over the Tibetan Plateau: Insights From HR-ToF-AMS and Aethalometer Measurements, J. Geophys. Res. Atmos., 126, 10.1029/2021jd035562, 2021.

Zhao, W., Zhang, X., Zhai, L., Shen, X., and Xu, J.: Chemical characterization and sources of submicron aerosols in Lhasa on the Qinghai–Tibet Plateau: Insights from high-resolution mass spectrometry, Sci. Total Environ., 815, 10.1016/j.scitotenv.2021.152866, 2022.

Zhao, Z., Cao, J., Shen, Z., Xu, B., Zhu, C., Chen, L.-W. A., Su, X., Liu, S., Han, Y., Wang, G., and Ho, K.: Aerosol particles at a high-altitude site on the Southeast Tibetan Plateau, China: Implications for pollution transport from South Asia, J. Geophys. Res. Atmos., 118, 11360-11375, 10.1002/jgrd.50599, 2013.

Zheng, J., Hu, M., Du, Z., Shang, D., Gong, Z., Qin, Y., Fang, J., Gu, F., Li, M., Peng, J., Li, J., Zhang, Y., Huang, X., He, L., Wu, Y., and Guo, S.: Influence of biomass burning from South Asia at a high-altitude mountain receptor site in China, Atmos. Chem. Phys., 17, 6853-6864, 10.5194/acp-17-6853-2017, 2017.

Zhou, S., Collier, S., Jaffe, D. A., Briggs, N. L., Hee, J., Sedlacek Iii, A. J., Kleinman, L., Onasch, T. B., and Zhang, Q.: Regional influence of wildfires on aerosol chemistry in the western US and insights into atmospheric aging of biomass burning organic aerosol, Atmos. Chem. Phys., 17, 2477-2493, 10.5194/acp-17-2477-2017, 2017.

Zhou, T., and Zhang, W.: Anthropogenic warming of Tibetan Plateau and constrained future projection, Environ. Res. Lett., 16, 044039, 10.1088/1748-9326/abede8, 2021.

Zhou, W., Xu, W., Kim, H., Zhang, Q., Fu, P., Worsnop, D. R., and Sun, Y.: A review of aerosol chemistry in Asia: insights from aerosol mass spectrometer measurements, Environ. Sci.: Proc. Imp., 10.1039/D0EM00212G, 2020.

Zhu, Q., He, L. Y., Huang, X. F., Cao, L. M., Gong, Z. H., Wang, C., Zhuang, X., and Hu, M.: Atmospheric aerosol compositions and sources at two national background sites in northern and southern China, Atmos. Chem. Phys., 16, 10283-10297, 10.5194/acp-16-10283-2016, 2016.

https://doi.org/10.5194/essd-2022-211
Preprint. Discussion started: 4 July 2022

Figures

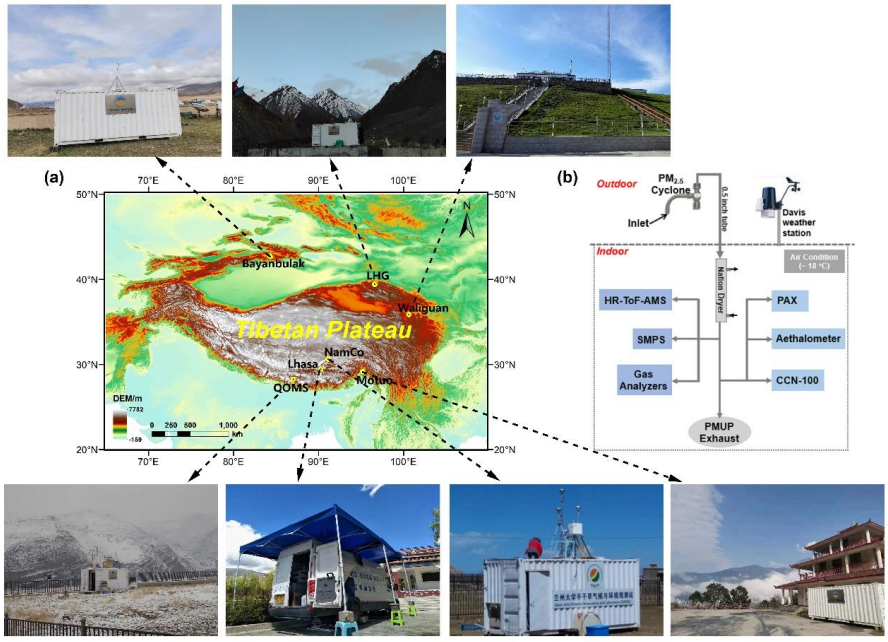

Figure 1. (a) Geographical locations of the observation sites (see Table 1 for full name and characteristics of each site) in the Tibetan Plateau and its surroundings in this study (The map is created with ArcGIS). Fieldwork photographs illustrate the real observation conditions and surroundings at each site. **(b)** The normal sampling setups of instruments during the online aerosol observations.

https://doi.org/10.5194/essd-2022-211
Preprint. Discussion started: 4 July 2022

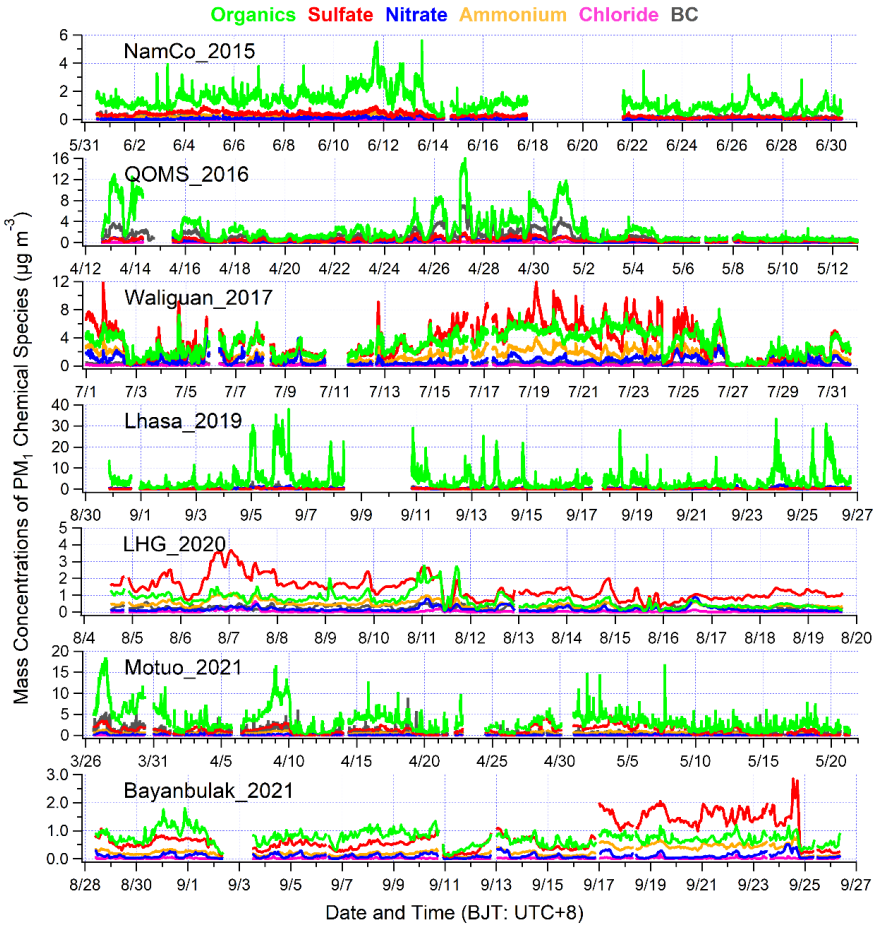

Figure 2. High-time-resolution temporal variations of the mass concentrations of PM_1 chemical compositions during the seven online aerosol field measurement campaigns over the Tibetan Plateau and its surroundings.

https://doi.org/10.5194/essd-2022-211
Preprint. Discussion started: 4 July 2022

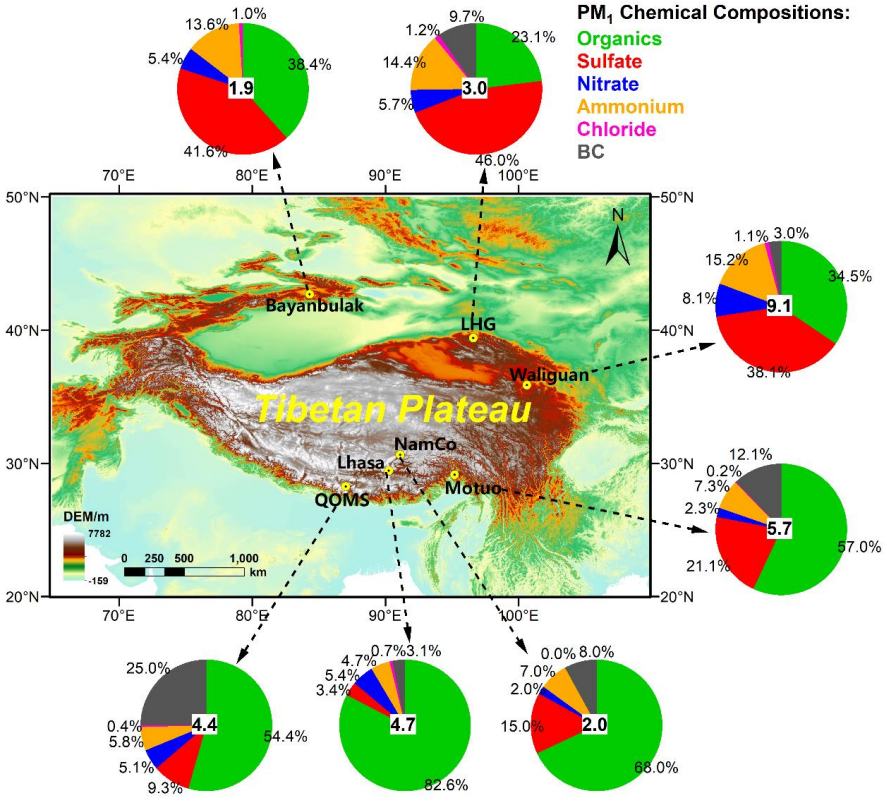

Figure 3. Regional distribution of average mass concentrations (values marked in the central of each pie chart with unit of μg m^{-3}) and chemical compositions (percentage values around each pie chart) of submicron aerosols (PM_1) during the seven online aerosol field measurements in the Tibetan Plateau and its surroundings (The map is created with ArcGIS).

https://doi.org/10.5194/essd-2022-211
Preprint. Discussion started: 4 July 2022

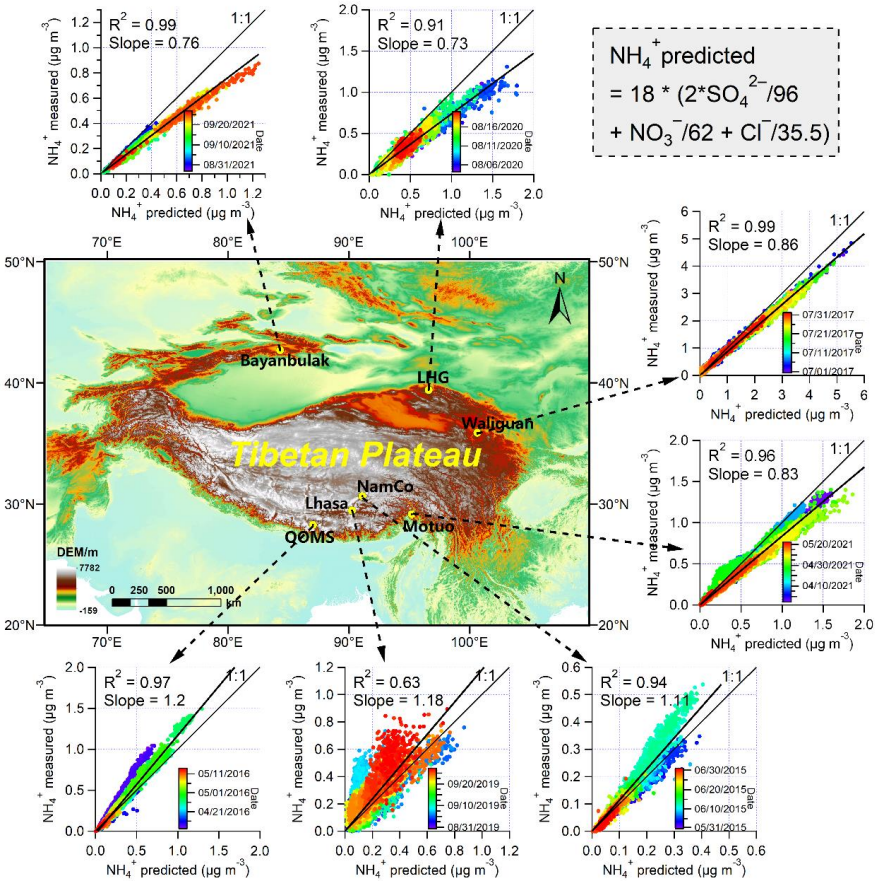

Figure 4. Regional difference of bulk acidity of submicron aerosols based on the scatterplot analysis and linear regression of measured NH_4^+ versus predicted NH_4^+ during the seven aerosol field measurement campaigns in the Tibetan Plateau and its surroundings (The map is created with ArcGIS).

https://doi.org/10.5194/essd-2022-211
Preprint. Discussion started: 4 July 2022

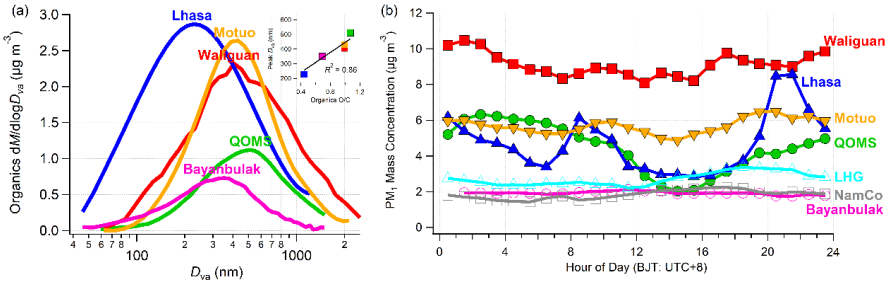

Figure 5. (a) Average size distributions of organic mass concentrations during five field measurement campaigns in the Tibetan Plateau and its surroundings. **(b)** Diurnal variations of total PM_1 mass concentrations during the seven field measurement campaigns in the Tibetan Plateau and its surroundings. Insert graph in **(a)** is the scatter plot of peak diameters in these size distributions versus the average O/C ratio of organics.

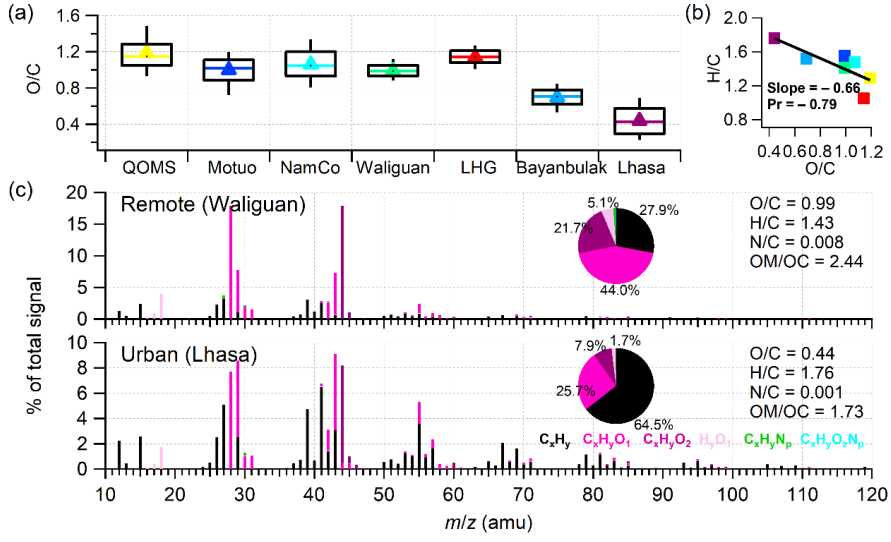

Figure 6. (a) Box plots of the average O/C ratios and **(b)** Van Krevelen diagram of H/C versus O/C among the seven field measurement campaigns in this study. **(c)** The average HRMSs of OA colored with different ion categories during the Waliguan and Lhasa measurement campaigns.

https://doi.org/10.5194/essd-2022-211
Preprint. Discussion started: 4 July 2022

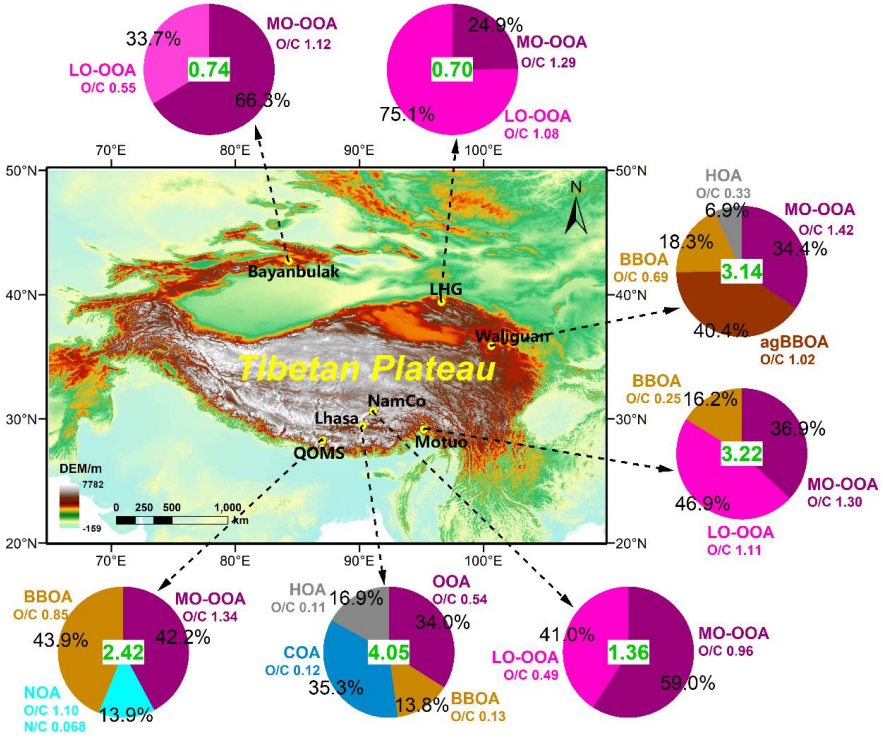

Figure 7. Regional distribution of OA components from PMF source apportionment during the seven online aerosol field measurements in the Tibetan Plateau and its surroundings (The map is created with ArcGIS). Values marked in the central of each pie chart are average OA mass with unit of μg m^{-3} while the percentage values around the pie chart are the mass contributions of each OA component. The O/C ratio of each OA component is also marked around each pie chart.

https://doi.org/10.5194/essd-2022-211
Preprint. Discussion started: 4 July 2022

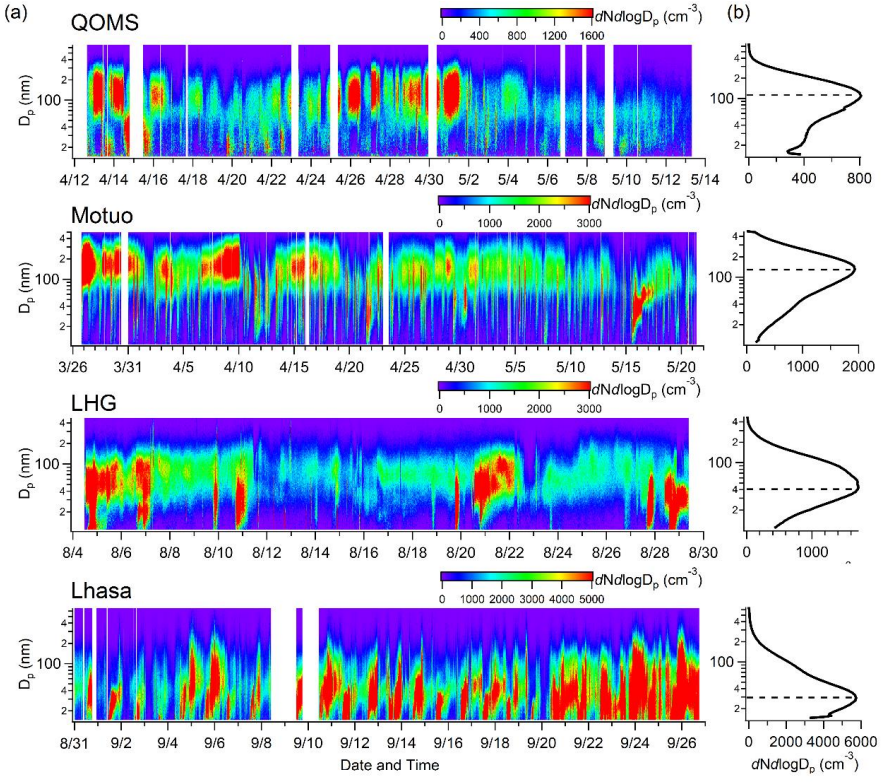

Figure 8. (a) Temporal variations of the size distributions of particle number concentrations during the aerosol field measurement campaigns at QOMS, Motuo, LHG, and Lhasa sites. **(b)** The average size distribution of particle number concentration during entire measurement period at each site.

https://doi.org/10.5194/essd-2022-211
Preprint. Discussion started: 4 July 2022

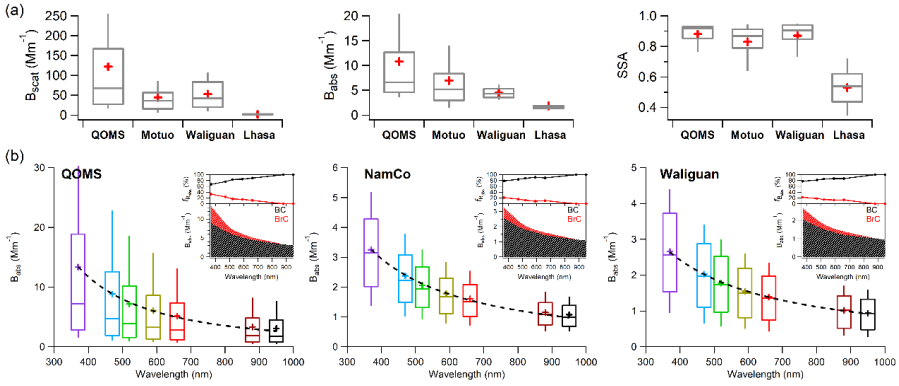

Figure 9. Box plots of **(a)** the average particle light scattering coefficient (B_{scat}), light absorption coefficient (B_{abs}), and single scattering albedo (SSA) during the four aerosol field measurement campaigns at QOMS, Motuo, Waliguan, and Lhasa sites, and **(b)** the particle B_{abs} at seven wavelengths measured by aethalometers at QOMS, NamCo, and Waliguan sites. The dashed lines in the boxes show the power-law fit of the average B_{abs} as a function of wavelength. The inserted plots in **(b)** are the apportioned contributions of BC and BrC to total B_{abs} at different wavelengths.

https://doi.org/10.5194/essd-2022-211
Preprint. Discussion started: 4 July 2022

Tables

Table 1. Detailed information about the full name and geographic characteristic of observation station, sample period, online instruments, and corresponding references during each aerosol field measurement campaigns over the Tibetan Plateau and its surroundings in this study.

Station	Full Station Name	Latitude (°N)	Longitude (°E)	Altitude (m)	Sample Period	Online Instruments							References
						HR-ToF-AMS		SMPS	PAX	Aethalometer	CCN-100	Gas Analyzers	
						MS	PToF						
QOMS	Qomolangma Station for Atmospheric and Environmental Observation and Research, Chinese Academy of Sciences	28.36	86.95	4276	12 April to 12 May 2016	√	√	√	√	√			Zhang et al. (2018) An et al. (2019) Xu et al. (2020) Zhang et al. (2021) Xu et al. (2022)
Motuo	Motuo County, Linzhi City, Tibet Autonomous Region, China	29.30	95.32	1305	26 Mar to 22 May 2021	√	√	√	√			√	In Preparation
NamCo	Nam Co Station for Multisphere Observation and Research, Chinese Academy of Sciences	30.77	90.95	4730	31 May to 1 July 2015	√				√			Xu et al. (2018) Zhang et al. (2021)
Waliguan	China Global Atmospheric Watch Baseline Observatory, Mount Waliguan Base	36.28	100.90	3816	1 July to 31 July 2017	√	√		√	√	√		Zhang et al. (2019) Zhang et al. (2020b) Xu et al. (2020) Zhang et al. (2021) Xu et al. (2022)
LHG	Qilian Observation and Research Station of Cryosphere and Ecologic Environment, Chinese Academy of Sciences	39.50	96.51	4180	4 August to 29 August 2020	√		√			√		In Preparation
Bayanbulak	Bayanbulak Town, Hejing County, Bayingolin Mongolian Autonomous Prefecture, Xinjiang Uygur Autonomous Region, China	42.83	84.35	2454	29 August to 26 September 2021	√	√						In Preparation
Lhasa	Lhasa City, Tibet Autonomous Region, China	29.65	91.03	3650	31 August to 26 September 2019	√	√	√	√			√	Zhao et al. (2022)

https://doi.org/10.5194/essd-2022-211
Preprint. Discussion started: 4 July 2022

Table 2. Summary of the average values measured with various instruments during the seven aerosol field measurement campaigns in the TP and its surroundings in this study.

Measurement items	QOMS	Motuo	NamCo	Waliguan	LHG	Bayanbulak	Lhasa
HR-ToF-AMS measurements							
PM_1 mass conc. (μg m^{-3})	4.4	5.7	2.0	9.1	3.0	1.9	4.7
PM_1 chemical compositions (%)							
OA	54.4	57.0	68.0	34.5	23.1	38.4	82.6
Sulfate	9.3	21.1	15.0	38.1	46.0	41.6	3.4
Nitrate	5.1	2.3	2.0	8.1	5.7	5.4	5.4
Ammonium	5.8	7.3	7.0	15.2	14.4	13.6	4.7
Chloride	0.4	0.2	0	1.1	1.2	1.0	0.7
BC	25.0	12.1	8.0	3.0	9.7		3.1
Peak diameter in mass size distribution (nm)	510.2	430.5		405.5		350.8	228.1
OA components (%)							
MO-OOA	42.2	36.9	59.0	34.4	24.9	66.3	
LO-OOA		46.9	41.0		75.1	33.7	
OOA							34.0
BBOA	3.9	16.2		18.3			13.8
agBBOA				40.4			
NOA	13.9						
HOA				6.9			16.9
COA							35.3
OA elemental ratios							
O/C	1.19	0.99	1.07	0.99	1.14	0.69	0.44
H/C	1.29	1.55	1.48	1.41	1.05	1.52	1.76
OM/OC	2.70	2.48	2.57	2.45	2.62	2.09	1.74
N/C	0.030	0.020	0.016	0.008	0.011	0.026	0.001
SMPS measurements							
Number conc. (cm^{-3})	709.3	1639.2			1462.0		3994.4
Peak diameter in PNSD (nm)	109.4	131.0			42.9		28.9
PAX measurements							
B_{scat} (Mm^{-1})	121.9	44.9		36.3			2.1
B_{abs} (Mm^{-1})	10.8	7.0		4.1			1.9
B_{ext} (Mm^{-1})	132.7	51.9		40.4			4.0
SSA	0.89	0.83		0.86			0.52
Aethalometer measurements							
$B_{abs,370}$ (Mm^{-1})	13.40		3.25	2.66			
Absorption Ångström exponent	1.73		1.28	1.12			
$B_{abs,BrC,370}$ (Mm^{-1})	4.42		0.69	0.60			
$B_{abs,BC,370}$ (Mm^{-1})	8.94		2.56	2.06			
$fB_{abs,BrC,370}$ (%)	33.1		21.3	22.4			
$fB_{abs,BC,370}$ (%)	66.9		78.7	77.6			
CCN-100 measurements (cm^{-3})							
CCN number conc. (*SS* 0.2%)				507.0	83.9		
CCN number conc. (*SS* 0.4%)				805.1	344.3		
CCN number conc. (*SS* 0.6%)				1073.3	429.9		
CCN number conc. (*SS* 0.8%)				1230.6	480.8		
CCN number conc. (*SS* 1.0%)				1336.6	516.1		
Gaseous pollutants measurements							
CO_2 conc. (ppm)		382.0					416.2
CO conc. (ppm)		0.47					
O_3 conc. (ppb)		33.5					36.7
SO_2 conc. (ppb)		3.0					9.8
NO conc. (ppb)		0.6					4.6
NO_2 conc. (ppb)		1.2					8.7
NO_x conc. (ppb)		1.8					13.3

https://doi.org/10.5194/essd-2022-211
Preprint. Discussion started: 4 July 2022

Table 3. Summary of the average PM_1 mass concentrations (μg m^{-3}) measured by the Aerodyne AMSs at various high-altitude and remote sites worldwide.

Observation Sites	Latitude (°N)	Longitude (°E)	Altitude (m a.s.l.)	PM_1 mass (μg m^{-3})	References
QOMS, China	28.36	86.95	4276	4.4	This study & Zhang et al. (2018)
Motuo, China	29.30	95.32	1305	5.7	This study
NamCo, China	30.77	90.95	4730	2.0	This study & Xu et al. (2018)
Waliguan, China	36.28	100.90	3816	9.1	This study & Zhang et al. (2019)
LHG, China	39.50	96.51	4180	3.0	This study
Bayanbulak, China	42.83	84.35	2454	1.9	This study
Lhasa, China	29.65	91.03	3650	4.7	This study & Zhao et al. (2022)
NamCo, China	30.77	90.95	4730	1.06	Wang et al. (2017)
Mt. Yulong, China	27.20	100.20	3410	5.7	Zheng et al. (2017)
Menyuan, China	37.61	101.26	3295	11.4	Du et al. (2015)
Mt. Wuzhi, China	18.84	109.49	958	10.9	Zhu et al. (2016)
Mt. Jungfraujoch, Switzerland	46.55	7.98	3580	0.55	Fröhlich et al. (2015)
Mt. Jungfraujoch, Switzerland	46.55	7.98	3580	2.24	Zhang et al. (2007a)
Mt. Bachelor, USA	43.98	-121.69	2800	15.10	Zhou et al. (2017)
Mt. Whistler, Canada	50.01	-122.95	2182	1.91	Sun et al. (2009)
Mt. Cimone, Italy	44.18	10.70	2165	4.5	Rinaldi et al. (2015)
Puy de Dôme, France	45.77	2.95	1465	5.58	Freney et al. (2011)
Sub-Antarctic Bird Island	-54.00	-38.04		0.46	Schmale et al. (2013)
Mace Head, Ireland	53.30	-9.80		1.53	Zhang et al. (2007a)
Hyytiala, Finland	61.90	24.30		2.04	Zhang et al. (2007a)
Storm Peak, USA	40.50	-106.70		2.11	Zhang et al. (2007a)
Duke Forest, USA	36.00	-79.10		2.82	Zhang et al. (2007a)
Chebogue, Canada	43.80	-66.10		2.91	Zhang et al. (2007a)
Okinawa Island, Japan	26.87	33.51		7.89	Jimenez et al. (2009)
Fukue Island, Japan	32.69	128.84		12.03	Takami et al. (2005)
Cheju Island, Korea	33.51	126.50		10.66	Jimenez et al. (2009)